

# Linking Deformation and Diffusion to Develop a Strain Speedometer

Naomi A. Barshi

Master of Science

Earth and Planetary Sciences

McGill University  
Montréal, Québec

A thesis submitted to McGill University in partial fulfillment of the requirements of the degree of  
Master of Science

© Naomi Barshi 2015

---

## Acknowledgements

---

Juliet García said in her 2015 commencement address to Smith College that there is only space on the diploma for the graduate's name. Likewise there is only space on the title page of this thesis for my name. Luckily there is space here to thank everyone who has made this project possible. First and foremost, I thank my master's supervisors, Christie Rowe and Vincent van Hinsberg, whose names appropriately appear on the manuscripts. Yajing Liu has also served as a helpful and resourceful committee member. Hours of science support from instrument technicians Lang Shi (Microprobe, McGill University) and André Poirier (LA-ICP-MS, UQÀM/Géotop) made the project possible. This thesis was greatly improved by the careful reading and insightful comments of Professor John Stix, my external examiner. Merci beaucoup à Jeanne Paquette, Louise Marie Meunier, et Matthew Tarling pour la traduction de l'abrégé.

My research group-mates and officemates have supported my frustrations, read my drafts, and answered my endless questions: Nils Backeberg, Charlie Beard, Nick Harrichhausen, Ben Melosh, Christine Regalla, Karin Siegel, Matthew Tarling, Sri Budhi Utami, and Longbo Yang. Charlotte Bate circled hundreds of plagioclase phenocrysts in one sample. Many other McGillians have been very helpful in bouncing ideas and asking me hard questions, especially Lucas Kavanagh, Jason Coumans, and Becky Paisely. Further science discussions with Scott Johnson, Heather Short, John Brady, Mark Pearce, Laurel Goodwin, Bob Martin, Ben Freiman, and many other conference attendees fuelled new ways of looking at my project. Matt Paulson was our extremely well-equipped

master camper field assistant, and we thank the friendly family at Rancho El Coral Falso for letting us camp safely on their beautiful land.

The rest of the McGill University Department of Earth and Planetary Sciences has also been of great support. In particular, administrative magic by Anne Kosowski, Brandon Bray, Angel Di Ninno, Kristy Thornton, and Nancy Secondo was invaluable. Brigitte Dionne printed my posters, which allowed my science to move forward with feedback at conferences. Kim Berlo and John Stix generously shared their spaces and facilities, including the cathodoluminescence microscope. Marcus Kunzmann helped with many  $\text{\LaTeX}$  questions and created the thesis template I adapted.

Funding came from grants from the Natural Science and Engineering Research Council of Canada (NSERC) to Vincent van Hinsberg and Christie Rowe, from the Fond de Recherche du Québec – Nature et Technologies (FRQNT) and a Robert Wares Fellowship to Christie Rowe, and from GEOTOP and a Graduate Research Enhancement and Travel Award from McGill University.

My parents have read drafts and heard hours of my attempts to translate my work into understandable words in their unwavering encouragement of my passion for learning. Thanks to Emmy Howard and Jim, Lucas, and Eva Markham for their hospitality, treehouse, and cats while I tied up loose ends. I have many other friends to thank at McGill and beyond. The list is too long and the words insufficient to express my gratitude for the support. I particularly acknowledge Katie Castagno, Lilly Dalton, and Monica Rolls, the Dream Team even during the nightmares.

---

## Contents

---

<b>Abstract</b>	<b>xi</b>
<b>Abrégé</b>	<b>xiii</b>
<b>Preface and Contribution of Authors</b>	<b>2</b>
Thesis Framework . . . . .	2
Contribution of Authors . . . . .	3
<b>1 Introduction</b>	<b>4</b>
1.1 Previous Work in Strain Speedometry . . . . .	5
<b>2 Theoretical Underpinnings</b>	<b>7</b>
2.1 Introduction . . . . .	7
2.2 Atomic Motion in Crystalline Solids . . . . .	8
2.2.1 Atomic Mobility Due to Chemical Gradients: Diffusion . . . . .	9
2.2.2 Atomic Motion Due to Stress: Shape Change . . . . .	11
2.2.3 Diffusional and Deformational Atomic Movement: Comparison and Interplay . . . . .	13
2.3 Beyond the Ideal Lattice . . . . .	15
2.3.1 Point Defects . . . . .	15

2.3.2	Lattice-Scale Defects . . . . .	16
2.3.3	Grain Boundary Element Mobility . . . . .	17
2.3.4	Lattice Defects, Deformation, and Element Mobility . . . . .	17
2.4	Comparing Activation Energies . . . . .	18
2.5	Documented Deformation-Enhanced Chemical Diffusion . . . . .	20
2.5.1	Metals . . . . .	20
2.5.2	Silicate Minerals . . . . .	20
2.6	Implications of Deformation-Enhanced Diffusion . . . . .	22
2.6.1	Geothermobarometry and Isotope Geochronology . . . . .	23
2.6.2	Strain Speedometry . . . . .	23
2.7	Conclusion . . . . .	27
<b>3</b>	<b>From Theory to Practical Application</b>	<b>28</b>
<b>4</b>	<b>Can We Measure Deformation-Enhanced Element Mobility in Naturally-Deformed Plagioclase?</b>	<b>29</b>
4.1	Introduction . . . . .	29
4.2	Approach . . . . .	30
4.2.1	Chemical Analytical Methods . . . . .	30
4.3	Field-Scale Studies . . . . .	31
4.3.1	Geologic Setting . . . . .	31
4.3.2	Evolution from Magmatic to Gneissic Fabric . . . . .	33
4.4	Sample-Scale Studies . . . . .	40
4.4.1	Quantitative Methods . . . . .	40
4.4.2	Quantifiable Changes . . . . .	46
4.5	Grain-Scale Studies . . . . .	48
4.5.1	Grain Selection . . . . .	48
4.5.2	Strain Measurements in Individual Phenocrysts . . . . .	50
4.5.3	Major Element Profiles . . . . .	52
4.5.4	Minor and Trace Element Profiles . . . . .	53

4.6	Evaluating Whether We Measured Deformation-Enhanced Element Mobility . . . . .	55
4.6.1	Field Scale Conditions . . . . .	55
4.6.2	Grain Scale Conditions . . . . .	61
4.6.3	Pluton Cooling . . . . .	62
4.7	Conclusions and Implications . . . . .	62
<b>5</b>	<b>Concluding Questions and Future Work</b>	<b>64</b>
	<b>Bibliography</b>	<b>71</b>
	<b>Appendices</b>	<b>73</b>

---

List of Tables

---

4.1	Correlations Between Grain Shape and Distance for Pluton's Edge . . . . .	46
4.2	Thermobarometry Results . . . . .	60

---

## List of Figures

---

2.1	Atomic Motion Takes Energy . . . . .	9
2.2	Vacancy and Atomic Motion . . . . .	10
2.3	Lattice Defects: Line Defects . . . . .	16
2.4	Lattice Defects: Grain Boundaries . . . . .	17
2.5	Activation Energies in Quartz . . . . .	19
2.6	Activation Energies in Plagioclase . . . . .	19
2.7	Schematic: Smoothed Diffusion Profiles . . . . .	24
4.1	Geologic Setting . . . . .	34
4.2	Field-Scale Evolution of Rock Fabric . . . . .	35
4.3	Biotite and Hornblende Alignments (stereonet) . . . . .	38
4.4	Biotite and Hornblende Alignments (field photo) . . . . .	38
4.5	Field-Scale Sample Descriptions . . . . .	41
4.6	Microstructural Sample Descriptions . . . . .	42
4.7	The $R_f/\phi$ Method . . . . .	45
4.8	Quantitative Changes in Plagioclase Phenocrysts . . . . .	47
4.9	Quantitative Changes in Aggregated Mafic Phases . . . . .	47
4.10	Plagioclase Shape ( $R_f/\phi$ ) Results . . . . .	49
4.11	Plagioclase Grains Analyzed . . . . .	51

4.12 Measuring Strain at the Grain Scale . . . . .	52
4.13 MTL Ca Profiles . . . . .	53
4.14 BTW Ca Profiles . . . . .	54
4.15 MTL Sr Profiles . . . . .	55
4.16 BTW Sr Profiles . . . . .	56
4.17 Thermobarometry Results . . . . .	60
4.18 Diffusion Profile Modelled for Cooling . . . . .	63
5.1 Remaining Questions . . . . .	65

---

## Abstract

---

I present the first comprehensive study of strain-enhanced diffusion in plagioclase through a multiscale, theoretical and physical approach. First I argue from first principles that diffusion and deformation are both processes of breaking and reforming bonds that take energy in order to proceed. Deformation can enhance diffusion by supplying strain energy that facilitates breaking bonds and by mobilizing dislocations, which can act as pathways for atomic migration. Widely-used geologic tools such as geochronometers and geothermobarometers neglect deformation-enhanced diffusion, which may lower closure temperatures and reset ages, temperatures, and pressures, leading to erroneous values calculated based on static diffusion or no diffusion after conditions of interest. If deformation enhancement of element mobility is measurable, we may be able to calculate and account for the effects of deformation on these calculations. The connection between deformation and diffusion also provides an opportunity to link deformation with a time-dependent process and infer strain rate. Strain rate is an integral parameter in understanding crustal deformation and cannot be directly determined from the rock record in most cases. To evaluate strain-enhanced diffusion in a common rock forming mineral, I combined field-scale, thin-section scale, and grain-scale strain and chemical measurements for major and trace elements in naturally deformed plagioclase phenocrysts from the San José Pluton, Peninsular Ranges Batholith, México. The multiscale approach made it possible to connect grain-scale strain with bulk-rock deformation through methods I developed. I used high spatial resolution, sensitive, *in situ* analyses using electron probe micro-analysis (EPMA) and Laser

Ablation Inductively Coupled Plasma Mass Spectrometry (LA-ICP-MS) to correlate changes in shape (strain) and chemical composition (element mobility). I conclude that at low strain and low compositional contrast between primary growth zones measured, the effect of strain-enhanced element mobility, as predicted from my model, is too subtle to quantify using available analytical techniques. This means that for such a set of conditions, a static diffusion model is sufficient, and geothermobarometers and geochronometers can still be applied to yield accurate results. Future work should explore the relationships between different variables affecting strain-enhanced element mobility, such as thermal history, strain, strain rate, and starting compositions, to refine the applicability of existing tools and the potential for new ones.

Je présente la première étude qui évalue en détail l'effet de la déformation sur l'augmentation des taux de diffusion des éléments dans la plagioclase grâce à une combinaison d'analyses théoriques et physiques à diverses échelles spatiales. En théorie, la déformation et la diffusion sont des processus qui requièrent que des liaisons atomiques soient rompues et reformées et dépendent donc d'un apport d'énergie. La déformation peut toutefois augmenter la vitesse de diffusion par l'addition d'énergie élastique, facilitant la rupture des liaisons atomiques et la mobilisation des dislocations qui favorisent la migration atomique. Les géochronomètres et géothermobaromètres sont des outils couramment appliqués sans inclure l'effet de la déformation sur la diffusion atomique, qui peut diminuer les températures de fermeture et remettre au zéro les horloges isotopiques. Des valeurs erronées de température et pression peuvent résulter de calculs basés sur le postulat d'une diffusion strictement statique ou négligeable sous les conditions estimées de température et pressions estimées.

Si l'augmentation de la mobilité des éléments par déformation est mesurable, nous pouvons en principe en corriger les effets sur les calculs de température et de pression. Le lien entre déformation et diffusion a également une dépendance temporelle qui nous permet de déterminer le taux de déformation des roches. Évaluer ce taux est essentiel à notre compréhension de la déformation crustale mais il est rarement possible de le déduire directement à partir des observations de terrain.

Pour évaluer l'augmentation des taux de diffusion due à la déformation d'un minéral crustal commun, j'ai combiné levés de terrain et analyses en lames minces pour décrire la déformation et la

---

composition chimique (éléments majeurs et en trace) de phénocristaux de plagioclase provenant du pluton San José, dans le batholite Peninsular Ranges au Mexique. J'ai développé une méthodologie me permettant de comparer le degré de déformation subi par ces grains individuels à celui de la roche qui les contient. J'ai évalué la déformation des grains par leur changement de forme et la mobilité de leurs éléments par la variation spatiale de leur composition chimique, mesurée à haute résolution par microsonde électronique et par spectrométrie de masse couplée à un plasma inductif avec prélèvement par ablation laser. Etant donné les modestes différences de composition observées entre les zones de croissance primaires des phénocristaux, mon modèle prédit que l'effet de la faible déformation subie par ces roches sur les taux de diffusion d'éléments dans la plagioclase est trop subtil pour être détecté par les techniques analytiques disponibles. Sous les conditions de déformation inférées pour ces roches, un modèle de diffusion statique est donc suffisant et les résultats d'outils comme les géothermobaromètres et géochronomètres sont valides. Il serait intéressant dans le futur d'explorer les relations entre divers facteurs, dont l'histoire thermique, le taux de déformation et la composition initiale de roches crustales, qui sont susceptibles d'influencer l'effet de la déformation sur la mobilité des éléments.

## Thesis Framework

In Chapter 2, I show, from first principles, that deformation enhances diffusion in a predictable, potentially measurable way, based on previous work in material science as well as geology. Mine is the first extensive geology-based exploration of strain-enhanced diffusion with an evaluation of potential impacts on current and future diffusion-based geologic tools. The second half of my project, presented in Chapter 4, is the application of this theoretical background: I endeavoured to measure strain-enhanced element mobility in feldspar minerals in order to develop a strain speedometer in a geologically important, nearly ubiquitous mineral. Feldspars are the most common mineral in crustal rocks and commonly control bulk-rock deformation. Measurable strain-enhanced diffusion in feldspar would support a new method to infer strain rate from the rock record and expand the geologist's toolbox. However, I found strain enhancement is below the detection limit of present state-of-the-art analytical instruments. This indicates that mineral-based thermobarometers and chronometers which do not account for strain enhancement of element mobility can still be applied to deformed rocks in low strain settings.

---

## Contribution of Authors

My advisors, Dr. Christie Rowe and Dr. Vincent van Hinsberg, jointly devised the basis for this project. Since beginning work on the project, I have taken the lead in all aspects: general project design, data collection and interpretation, presentation of results at numerous conferences, and finally writing this thesis. I worked through the mathematical connections presented in Chapter 2 on my own, but conceptual links were a collaborative effort with frequent re-working driven by Dr. van Hinsberg. The practical work to apply our ideas was primarily mine, with generous support from my advisors. We worked together to select and develop meaningful analyses for structural and chemical measurements, including instrument set-up. I collected the samples and field measurements with assistance from Dr. Rowe and Matt Paulson. I selected and cut my rock samples and developed methods to image them. I conducted all the analyses with minor assistance and received generous advice in processing the data. In all written aspects of this project, my advisors have provided lucid feedback, including some specific phrasing suggestions which I have incorporated. As such, their names are listed as co-authors in order of contribution on each manuscript, and I use first person plural throughout the manuscripts.

# CHAPTER 1

---

## Introduction

---

Deformation in Earth's crust ranges from stretched bonds between atoms in mineral lattices to folds of hundreds of kilometers of rock in mountains. The geologist's toolkit includes myriad methods to unlock the histories of change in pressure, temperature, chemistry, texture, and shape at all these scales of time and space (Spear, 1993). A recent surge in research has revived efforts to develop speedometers to track the rates at which earth processes change these variables (Grove, 1982; Blackburn et al., 2012; Strandmann et al., 2015). Because time travel has yet to be refined outside of fiction, geologists must rely on the evidence left in the rock record to infer the temporal dimension of the past. One time-dependent process which has been used as the basis for speedometers is diffusion: the motion of elements inside a crystal lattice driven by a compositional gradient (Zellmer et al., 2003). One speedometer sorely lacking in the toolbox is a deformation speedometer. It remains unknown at what rates and in what fashion crustal deformation proceeds over long timescales. Is it episodic, periodic, protracted, fast? This rate, specifically called strain rate, is an important parameter governing the response of rocks to stress. Deformation is also a process of atomic motion, and in this thesis I investigate the fundamental similarities of diffusion and deformation to develop a strain speedometer.

## 1.1 Previous Work in Strain Speedometry

Present methods for characterizing strain rate are limited by specific requirements of composition, deformation conditions, and other parameters, including grain size. Generally, these approaches involve inferring differential stresses active during deformation from textural or crystallographic properties, then calculating strain rate from experimentally developed flow laws (rheological relationships between stress, strain, and strain rate). For example, temperature-constrained quartz paleopiezometry (Stipp and Tullis, 2003) uses recrystallized quartz grain size to infer flow stress based on experimental calibration. This method is useful when quartz is the primary mineral that controls the way the rock responds to stress, such as in quartzites, and dislocation creep is the primary deformation mechanism. Stipp and Tullis (2003) report that their method worked best on grain sizes of  $\sim 3 - 45\mu\text{m}$ . This method is not applicable to polyphase rocks with larger grain size.

Determining dominant deformation mechanisms based on crystallographic preferred orientations (CPO) is another method to infer strain rate. Crystallographic preferred orientations are measured using electron backscatter diffraction (EBSD). Different groupings of orientations indicate movement along differing slip systems activated by different deformation mechanisms initiated at different strain rates (e.g. Prior et al., 1999; Law et al., 1990). The minerals used to estimate pressure and temperature conditions are often accessory phases and not the minerals used to determine dominant deformation mechanisms. This may yield discrepant results if different minerals responded differently to deformation conditions.

In some cases, directly dateable syn-tectonic features such as dikes or growing minerals are deformed such that the quantity and timing of deformation can be precisely constrained. Sassier et al. (2009) dated dikes that cooled quickly as they intruded an active shear zone. Since strain rate is defined as the time-derivative of strain, measurement of strain in increasingly deformed dikes and the time from first to last intrusion allows for a direct calculation of strain rate. Other passive strain markers that can be dated are minerals that grow as they are deformed. Garnet is a common mineral in metasedimentary and some meta-igneous rocks and is more resistant to deformation than quartz, feldspar, and micas. Dating growth of new garnet zones as the garnets rotate during deformation-accompanied metamorphism provides coupled strain and time measurements from which strain rate can be calculated (Müller et al., 2000; Christensen et al., 1994). However, both

these measurements require dateable features and/or specific mineralogy and focus on minerals that do not represent bulk rock strain. Moreover, resolution of geochronological methods is on the scale of tens to hundreds of thousands of years, so only conditions of low strain rates work for these investigations.

---

Theoretical Underpinnings: Uniting Element Mobility Processes *ab Initio*  
Demonstrates Deformation Enhances Diffusion

---

Naomi Barshi, Vincent van Hinsberg, and Christie Rowe

## 2.1 Introduction

Micro-scale mobility of atoms governs macro-scale changes in the shape of minerals and rocks, which is deformation. If this mobility involves different atoms, it will lead to change in mineral composition, referred to as diffusion. Deformation and diffusion have each been extensively studied, generally from disparate perspectives that rarely explore the commonalities of these processes of atomic migration. A link between deformation and diffusion has been established for decades, particularly in materials science (e.g. Love, 1964; Cohen, 1970), but a first-principles review in the context of geology has been lacking despite several studies seeking to measure strain-enhanced diffusion (e.g. Yund et al., 1981; Büttner, 2005; Reddy et al., 2006). We first explore deformation and diffusion from first principles as processes of breaking and reforming bonds in a crystal lattice in order to establish that strain enhances element mobility. We present a new, *ab initio* logical argument for deformation-enhanced element mobility in minerals. In the second portion of the paper, we

present previous work documenting measurable enhancement of element mobility by deformation. We conclude the paper with ramifications for current and future petrologic applications.

## 2.2 Atomic Motion in Crystalline Solids

Atoms move in a crystal lattice in response to a driving force. Their mobility continues until a steady-state equilibrium has been attained. A variety of driving forces exists in natural systems, the most important of which are gradients in 1) temperature, 2) composition, and 3) stress. We explore the similarities between the latter two and the resulting macroscopic effects of element diffusion and lattice deformation, respectively.

An atom can move through a crystal lattice by a variety of mechanisms (e.g. Porter and Easterling, 1989; Zhang, 2010), most basically by trading places with a vacancy in the lattice (Fig. 2.1). From an atomistic perspective, each atom is in motion at temperatures above absolute zero (0 K). If the atom is in a lattice site, a large enough vibration allows it to escape its site and move. The probability of atomic motion increases as a function of this vibrational energy until it reaches 1. However, mobility takes place at all vibrational energies and is only impossible at 0 K. Therefore it is more useful to talk about the energy and the associated threshold probability at which significant mobility occurs. Different factors including temperature and other external energy inputs contribute to the vibrational energy and the shape of the probability distribution. This atom mobility leads to macroscopic deformation and diffusion. In a microscopic phenomenological model to fit macroscopic observations, the parameter  $E_{\text{Act}}$ , the *activation energy*, accounts for the atomic energy involved in atomic motion. Although there is a range of energetic states at which an atom can move, a single value is used to fit phenomenological models.

The change in energy as an atom moves through the lattice can be visualized as an oscillating function in the context of transition state theory (Fig. 2.1, Zhang, 2008). The energy state of the lattice is lower before and after the vacancy and atom have traded places than it is while the atom breaks its surrounding bonds and “squeezes” through the lattice (the transition state). The height of these energy hills that atoms must overcome in order to move is  $E_{\text{Act}}$ . The higher the activation energy, the less likely an atom has the required energy to overcome it, and, therefore, the harder it is for an atom to move. Activation energies are both element- and mineral-specific: they depend on

the properties of the atom (e.g. its electronic structure and radius) and lattice (e.g. lattice elasticity, density of atom packing) (Dowty, 1980). In general, larger atoms and lattices whose bonds are stronger or atoms more closely packed have higher activation energies so show less element mobility. In macroscopic terms, such a lattice in which atoms have more difficulty moving would thus display less deformation, and larger atoms less diffusion, which is indeed observed (Brady and Cherniak, 2010; Ranalli, 1995; Fortier and Giletti, 1989; Van Orman et al., 2001). We use the notation  $E_{\text{Act}}$  to refer to the general concept of activation energy and specify different activation energies for different processes separately.

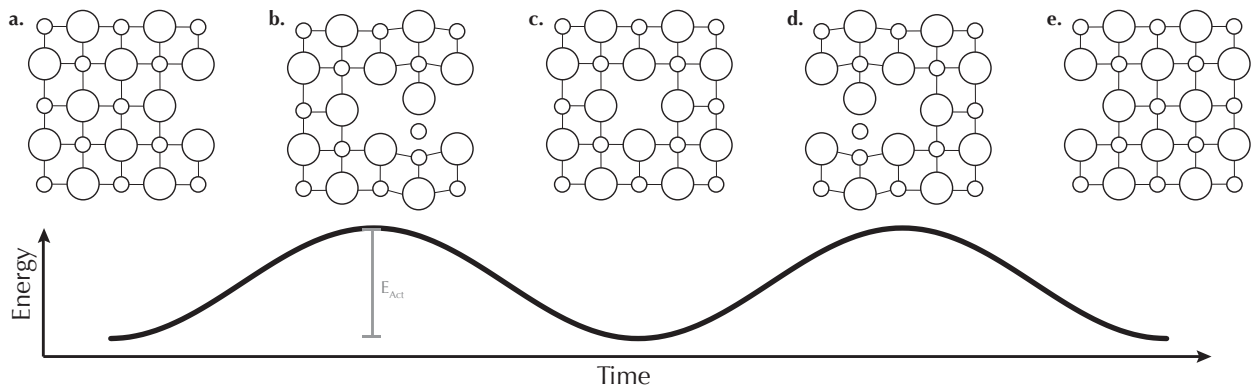


**Figure 2.1** Atoms and vacancies move through a crystal lattice. Each snapshot has a different energy state. **a.)** A lattice with one vacancy at an initial energy state. **b.)** The middle atom in the lattice “squeezing” between its neighbours. This is the highest energy state of atomic motion. **c.)** The atom settles into a lattice site once more. The vacancy has now shifted into the atom’s initial site. **d.)** An equivalent state to *b*, but with the next atom. **e.)** The final state after two atoms and two vacancies have traded places. (Figure inspired by Ranalli (1995); Nicolas and Poirier (1976).)

### 2.2.1 Atomic Mobility Due to Chemical Gradients: Diffusion

Atomic motion of elements in a crystal lattice can be driven by chemical potential gradients, that is, by a higher concentration of an element or vacancy on one side of the crystal lattice (Zhang, 2010). In the atomistic perspective, this makes the probability of atomic motion more likely in certain directions. For the purpose of this discussion, we retain the microscopic rather than the atomistic perspective. Consider a perfect, isolated lattice (Fig. 2.2a) in which a chemical gradient is introduced by adding 7 vacancies (Fig. 2.2b). The concentration of vacancies in the top left corner has a vacancy gradient away from it, which provides a driving force for element mobility. The intervening high energy stages (illustrated in Figure 2.1) are omitted for clarity.



Atoms and vacancies subsequently swap places, preferentially down the chemical gradient (2.2c-g), ultimately approaching an equilibrium distribution with an equal concentration of atoms and vacancies throughout the lattice (Fig.2.2h). The net migration of matter and space in either case is accomplished by opposite fluxes of atoms and vacancies. Fick (1855) described this flux ( $J$ ) as the rate of change of the concentration ( $C$ ) of either vacancies or atoms with respect to distance ( $x$ ), scaled by the diffusion coefficient ( $D$ ) Though diffusion happens in three dimensions, consider just the x-direction in a Eulerian coordinate system:

$$J = -D \frac{\partial C}{\partial x} \quad (2.1)$$

The diffusion coefficient,  $D$ , is material-specific and controls the rate at which atoms move. It depends on the activation energy, described above, as well as temperature and material properties. An Arrhenius equation describes it phenomenologically:

$$D = D_0 \exp\left(-\frac{E_{\text{ActD}}}{RT}\right) \quad (2.2)$$

where  $D$  is the diffusion coefficient ( $m^2/s$ ),  $D_0$  is an experimentally determined parameter characteristic to each element in each material and the direction of motion in anisotropic media ( $m^2/s$ ),  $E_{\text{ActD}}$  is the activation energy specifically for diffusion, given in kJ/mol (the amplitude of the energy curve in Figure 2.1),  $R$  is the universal gas constant, and  $T$  is the temperature in K.

### 2.2.2 Atomic Motion Due to Stress: Shape Change

Chemical potential gradients drive atomic motion in a preferred direction, but the overall mineral-scale change in concentration does not result in a change in shape (c.f. Fig. 2.2c-h).<sup>1</sup> Stress is another driver of atom mobility and *does* result in a change in shape if the stress exceeds the strength of the material. When a constant, anisotropic stress is applied to the same vacancy-containing lattice as discussed above for diffusion (Fig. 2.2b), the bonds are elastically strained (Fig. 2.2i). Vacancies and atoms swap places parallel to the resolved shear stress direction (Fig. 2.2j-m), ultimately resulting in a lattice in which bonds are no longer strained (Fig. 2.2n). The final state illustrated has the same

---

<sup>1</sup>Note that this is true only for the simplified intra-grain case illustrated here.

vacancy concentration as the initial state but with a different lattice shape. This is the end-member case in which atom mobility leads to deformation without a change in concentration. Other results are also possible. The lattice may reach a local minimum strain energy state and atoms stop diffusing before reaching equilibrium, although such a metastable state is not possible in the idealized lattice drawn in Figure 2.2. Or, if viewed at the crystal scale, then the vacancies effectively disappear if they diffuse to the grain boundary. (The same is true for diffusion as a result of a chemical gradient.) If bulk lattice shape change is more efficient than static diffusion of atoms and vacancies (strain rate exceeds static diffusion rate), then more vacancies are created than destroyed, and the net concentration of vacancies increases. This in turn could further increase diffusion by providing more empty sites into which diffusing atoms can migrate. The relationship between strain rate and diffusion is not simple, and we explore it in more detail in Section 2.6.2.

Many different mechanisms operate in crystals that govern the specific means by which atoms migrate. The combined effect can be approximated by a power-law relationship between strain rate and stress (e.g. Poirier, 1985). In a compilation describing the characteristics of different deformation mechanisms for feldspar, Rybacki and Dresen (2004) use the generalized equation

$$\dot{\epsilon} = A\sigma^n d^{-m} \exp\left(-\frac{E_{\text{ActM}}}{RT}\right) \quad (2.3)$$

to describe the dependence of strain rate ( $\dot{\epsilon}$ ) on a material parameter that takes into account elasticity and other properties ( $A$ ), stress ( $\sigma$ ), grain size ( $d$ ), an activation energy for atomic migration for a particular deformation mechanism ( $E_{\text{ActM}}$ ), the gas constant ( $R$ ), and absolute temperature ( $T$ ). The exponents  $m$  and  $n$  vary for each deformation mechanism, but are simply numbers used to fit the flow law to observations.

This flow law describes the behaviour of polycrystalline, monomineralic rocks. We use it at the intra-grain scale because we are unaware of a single-crystal flow law and find this flow law instructive even if its derivation is at a different scale than we consider here. In the single-grain case, we consider the flow law to no longer depend on grain size ( $d$ ).

The similarity between Equation 2.3 and the combination of Equations 2.1 and 2.2

$(J = -D_0 \exp\left(-\frac{E_{\text{ActD}}}{RT}\right) \frac{\partial C}{\partial x})$  is striking:

$$\text{atomic motion rate} \propto \text{material characteristics} \cdot \text{driving mechanism} \cdot \exp\left(-\frac{E_{\text{Act}}}{RT}\right)$$

Activation energy for diffusion and deformation are not identical because the driving forces and material properties in the two equations differ. Still the activation energies are closely related. Both can be conceptualized as the energy required to initiate a process of change. Yet, except at absolute 0 K, the processes are already happening, if not significantly. Once conditions are such that the process can initiate beyond the threshold probability (T, P, V, all contribute), we consider it to be operating. In both diffusion and deformation, the core meaning—the vibrational energy an atom possesses that relates to its probability for motion—is an inherent atomic property and is therefore the same property affected by two different processes. In diffusion, a chemical potential gradient is the driving mechanism while in deformation a deviatoric stress (a force gradient over an area) is the cause. We discuss the implications of activation energy further in Section 2.4.

### 2.2.3 Diffusional and Deformational Atomic Movement:

#### Comparison and Interplay

The equations describing element mobility in idealized crystal lattices—whether driven by chemical potential resulting in distributed equilibrium arrangements of matter and space or localized rearrangements driven by stress—are of the same form. In both, the rate of change of the metric of motion (concentration for diffusion and shape for strain) is a function of the characteristics of the lattice and the mobile atom, expressed by a constant and an activation energy (Eqs. 2.2 and 2.3). This is not surprising after a careful investigation of Figure 2.2c-h and 2.2i-n. A similar number of bonds break in each process because a similar number of atoms move. The barriers to motion are the same, because the atoms and vacancies are identical. With these related activation energies and identical lattice and atom characteristics, under driving forces of equivalent magnitude at equal temperatures, the atom mobility must also be essentially identical. That is, in this simplified example, element mobility as a result of a chemical gradient is equivalent to mobility resulting from a stress gradient with the only difference being the final lattice shape. For anisotropic media, there is a directional preferred mobility and  $E_{\text{Act}}$  values vary with crystallographic orientation. Lattice

parameters, captured by the pre-exponential terms, are also anisotropic in this case. Diffusion and deformation then have a preferred orientation, and comparison between them is restricted to the same crystallographic direction. Stress is also anisotropic, and only the component along a given crystallographic direction could be considered as a driver for atom mobility.

We are not the first to draw this connection and establish the essential similarity of these processes (Cohen, 1970). However, the ramifications of this connection have been under-explored. We illustrate them here with reference to Figure 2.2.

Some of the bonds in Figure 2.2i are stretched. These strained bonds are closer to their elastic limit than the same bonds in the unstrained lattice. Given sufficient stress, the bond gets stretched beyond its elastic limit, the bond breaks, and the atom can jump to a nearby vacant site. In this way, strain contributes energy toward the total energy required to make the jump. Below the yield stress, the lattice is elastically strained (Fig. 2.2i). Because the vacancies in this lattice are concentrated in the top left corner, a chemical gradient also exists and also drives diffusion. Due to strain in the bonds, the diffusing atoms experience a lower activation energy in this lattice than in the unstrained lattice in Figure 2.2b. This makes atomic motion easier and enhances diffusion proportionally to the strain in the lattice, and, by extension, the applied stress. The higher the strain, the closer the bonds are to breaking, the lower the activation energy for atomic motion, and the faster the chemical gradient disappears. More simply, strain should enhance diffusion.

In a specific example, consider the energy contribution toward diffusion resulting from 1% strain of the Si-O bond in crystalline quartz at about 200 MPa. If the bond begins at 1.608 Å (Levien et al., 1980), it is 1.624 Å at its strained length. The elastic strain contributes 0.087 kJ/mol toward the 300 kJ/mol needed for diffusion of Si in quartz (Brady and Cherniak, 2010), based on an elastic (Young's) modulus of 68 GPa for quartz (Pabst and Gregorová, 2013) and the equation for elastic potential energy. At 400°C, strain allows atoms to move about 0.8% farther, and the effect becomes less pronounced with increasing temperature (see the Appendix for calculations). Given 1 Myr to diffuse at 400°C from an initial relative concentration contrast from 1 to 2, Si would travel about 0.0212  $\mu\text{m}$ . With 1% strain, this distance would increase to 0.0214, an increase of 0.9%. Ar would get 60.07  $\mu\text{m}$  in the same unstrained conditions and 60.54  $\mu\text{m}$  with 1% strain, an increase of 0.8%. Li, with even lower activation energy and faster diffusion rate (Brady and Cherniak, 2010), theoretically reaches 2.05 m in 1 Myr and 2.06 m under 1% strain in the same conditions, an increase of 0.5%.

While these may not be geologically meaningful measures, they serve to illustrate the differential increase of diffusion distance due to strain.

The effect of strain on element mobility is not limited to major elements. Impurity elements are present in natural minerals, with the same types of bonds and barriers to motion. These are affected by the interplay between deformation and diffusion which universally lowers activation energies for all atoms attached to strained bonds. Because the electronic and physical structure of impurity atoms are non-ideal for the lattice sites they occupy, impurity atoms already have lower activation energies for motion than the major elements in the crystal lattice (e.g. Brady and Cherniak, 2010; Cherniak, 2010). Thus, we suggest that the impact of strain-enhancement is even larger for impurity atoms than for stoichiometric atoms with higher activation energies because the same strain energy contribution brings them even closer to their energy goal than it does stoichiometric atoms to theirs. A relative acceleration of fast-diffusing elements should occur, and we explore the potential uses of this enhancement in Section 2.6 below.

## **2.3 Beyond the Ideal Lattice**

The idealized case of diffusion and deformation described above in two dimensions is very simplified compared to the complexity of natural crystals, which rarely, if ever, grow perfectly. Instead, they contain a variety of impurities and lattice defects, which greatly speed up mobility of elements. In this section, we discuss a variety of lattice defects and diffusion enhancement mechanisms. The same basic concepts outlined above hold in these more complex cases.

### **2.3.1 Point Defects**

We have already discussed vacancies, but non-stoichiometric atoms may also take the place of major elements as impurity atoms. One-dimensional lattice defects such as these are called point defects. Impurity atoms tend to have lower activation energies than the atoms for which they substitute (Brady and Cherniak, 2010). For any atom to move, it must trade places with a vacancy or with another atom. The presence of more impurity atoms, more easily disturbed from the lattice sites they occupy, increases the possibility for element mobility for all atoms due to bonds stretching or compressing to fit the non-ideal atoms (Blundy and Wood, 2003).

### 2.3.2 Lattice-Scale Defects

During growth or as a result of partial lattice slip, a lattice may incorporate a lattice mismatch called a dislocation (Fig. 2.3, which is essentially a 3D version of the defect shown in Fig. 2.2i-m). Dislocations can be extra half-planes of atoms (edge dislocation, Fig. 2.3a) or a rotation of part of the lattice along a plane (screw dislocation, Fig. 2.3b). In both cases, the extra space within the dislocation is an efficient travel pathway for migrating atoms (Love, 1964).

Dislocations are formed and mobilized during deformation. This further increases element mobility. As dislocations move, they expose more of the crystal to diffusion expressways (Yund et al., 1981). The moving dislocations visit more potentially diffusing atoms (Ruoff and Balluffi, 1963a). The cumulative effect of (directional) dislocation creep can amount to significant changes in crystal shape (e.g Poirier, 1985). Dislocations promote both diffusion and deformation, and the processes of diffusion and deformation retain the equivalence established above for the simplest case.

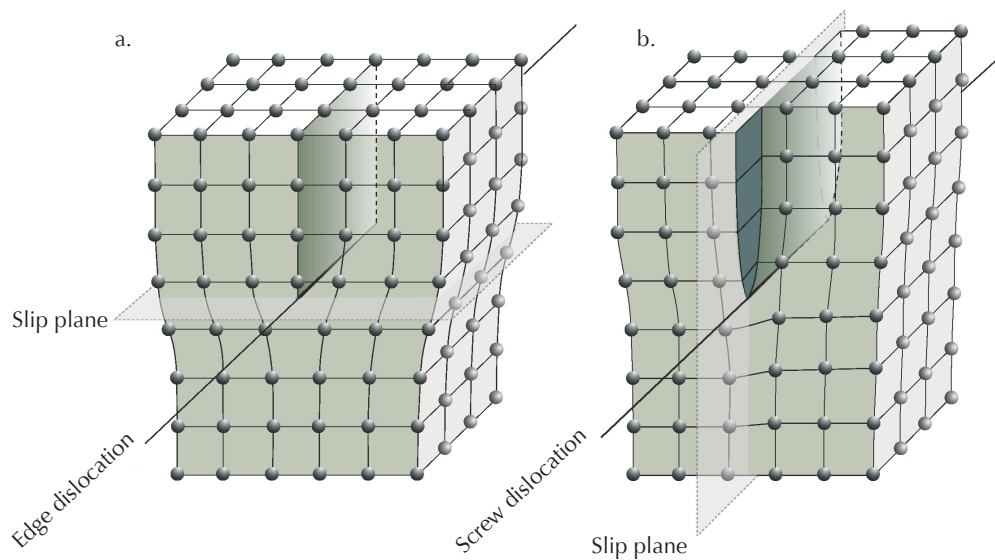


**Figure 2.3** An extra half-plane of atoms (a.) or rotational mismatch (b.) may be incorporated during crystal growth or may be the result of lattice slip. The resulting mismatch in the crystal lattice is an efficient travel path for migrating atoms, both because of strained bonds surrounding the dislocation and the extra space within the dislocation “pipe”. Figure 10.11 in Fossen (2010).

### 2.3.3 Grain Boundary Element Mobility

Grain boundaries can also be treated as lattice discontinuities which concentrate efficient atomic motion (Fig. 2.4 Ruoff and Balluffi, 1963a; Lee, 1995; Eiler et al., 1992). Like dislocations, the extra space between irregularities can be a space for elements to travel more efficiently. The irregular lattice edges are also replete with defects and impurities compared to grain interiors, which can further enhance diffusion rates (e.g. Brady, 1983). Like dislocations, grain boundaries can also be mobilized during deformation in grain boundary migration processes (e.g. Poirier, 1985).

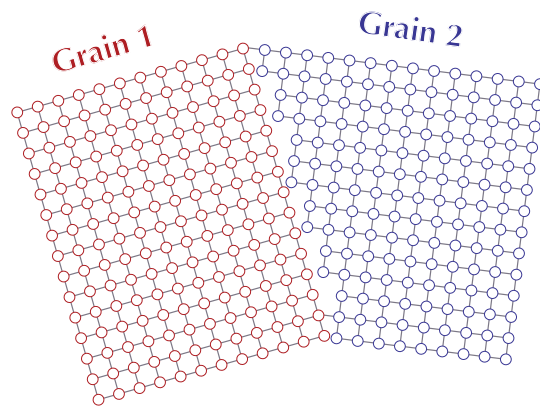


**Figure 2.4** Grain boundaries are three-dimensional mismatches between crystal lattices and provide efficient travel paths for elements both as static highways and as migrating travel paths during grain boundary migration processes.

### 2.3.4 Lattice Defects, Deformation, and Element Mobility

The relative importance of lattice defects and deformation processes for enhancing element mobility likely varies primarily with temperature, as evidenced by the equations describing these processes (Eqs. 2.2 and 2.3). Each aspect of defect formation, deformation, and energy required for all these processes is exponentially dependent on temperature. We hypothesize that the high-energy, lattice-scale, migrating high-diffusivity paths of dislocations mobilized during dislocation creep likely outpace stationary defects in enhancing element mobility. Investigations of deformation-enhanced element mobility, discussed in Section 2.5, also support this conjecture.

## 2.4 Comparing Activation Energies

The diffusion coefficients and deformation rates measured in the lab—and the activation energies calculated from them—represent the macro-scale amalgamated effects of several atomic mobility processes. For the combination of mineral, composition, pressure, temperature, fluid, grain size, stress, and rate conditions tested, a dominant process can usually be interpreted (e.g. Stipp et al., 2002; Hirth and Tullis, 1992). As previously discussed, the underlying processes governing element mobilities for diffusion and deformation are the same, and their equations comparable (Eqs. 2.2 and 2.3). As such, the activation energies derived from diffusion and deformation experiments ought to be similar. They are, taking into account the uncertainty of the mobility mechanism and differences in experimental conditions which affect element mobility (e.g. presence of water). Activation energies for deformation mechanisms are on par with those for diffusion of major elements, both in quartz (Fig. 2.5) and in the more complicated lattice of feldspar (Fig. 2.6). The similarity in the values indicates that the energy involved in permanent strain is sufficient to contribute to the energy required for diffusion and hence lead to enhanced diffusional element mobility during deformation. We suggest that the strain energy contribution is not a wholesale reduction of the total energy required for diffusion but rather a contribution toward the lattice-defined energy goal. This is analogous to a grant to make a purchase rather than a reduction in the price of the item. In the atomistic perspective, this can be described as strain increasing the vibrational energy of each atom, increasing its probability for motion. This further supports our thesis that from the atomistic perspective, both deformation and diffusion are equivalent and essentially the same process.

The activation energy for Si diffusion in quartz and NaSi-CaAl interdiffusion in feldspar is higher than that of trace elements within their respective lattices (Figs. 2.5 and 2.6). We hypothesize that a strain energy contribution to of the overall activation energy thus affect the trace elements with lower activation energies first and foremost, with those with the lowest activation energy seeing the largest increase in diffusion rate. Of the elements studied here, we predict that Ar will be affected first in quartz while in feldspar we expect Li to be affected first.

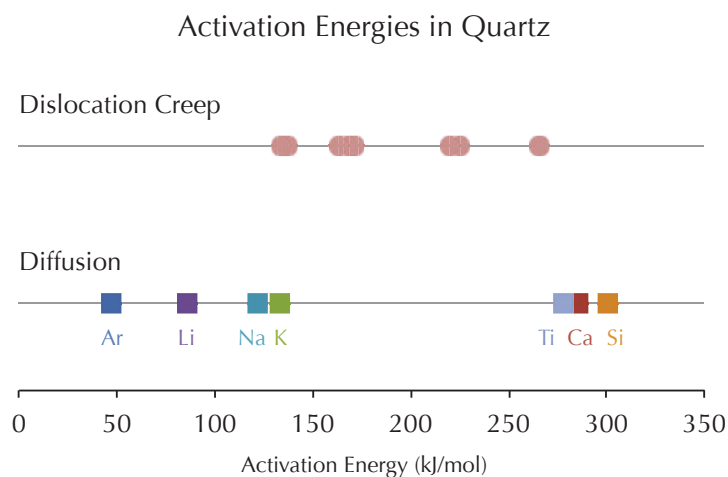
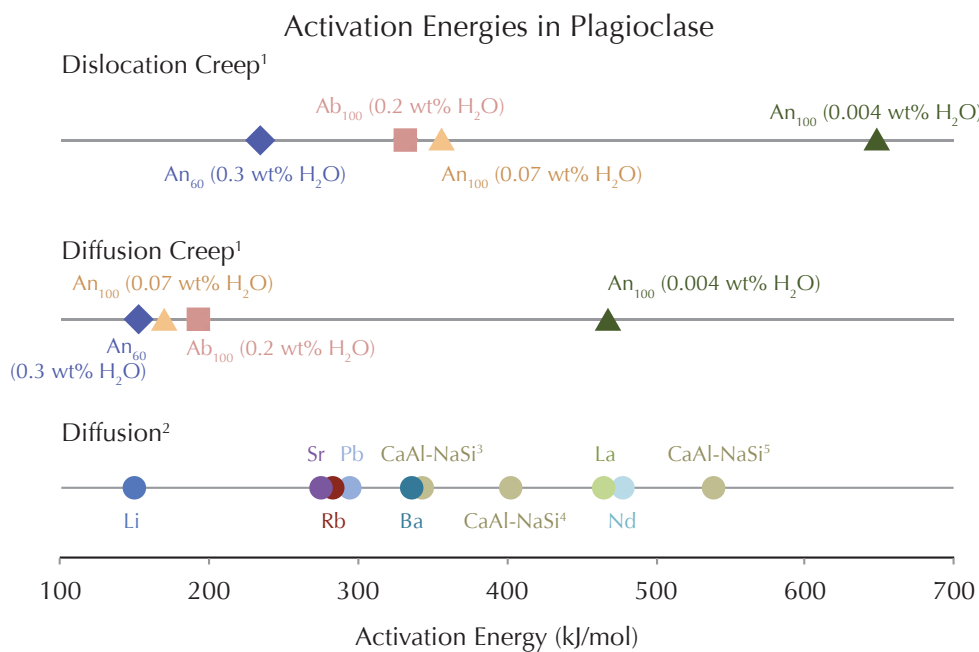


**Figure 2.5** Estimates of activation energy ( $E_{ActM}$ ) for dislocation creep in quartz from a range of experiments compiled by Gleason and Tullis (1995). Activation energies ( $E_{ActD}$ ) for diffusion of a variety of elements in quartz compiled by Brady and Cherniak (2010).



1. Rybacki and Dressen (2004)
2. Aggregated data for  $\sim$ An<sub>30</sub> from Brady and Cherniak (2010)
3. Interdiffusion in wet experiments (Liu and Yund, 1992)
4. Interdiffusion with 0.5 - 2 wt% water (Yund, 1989)
5. Interdiffusion experiments by Grove et al. (1984)

**Figure 2.6** Activation energies for two common deformation mechanisms ( $E_{ActM}$ ) and diffusion ( $E_{ActD}$ ) of several elements in plagioclase are shown here. Values from aggregated diffusion data (Brady and Cherniak, 2010) are averaged for intermediate plagioclase compositions.

## 2.5 Documented Deformation-Enhanced Chemical Diffusion

The complexity of mineral lattices far exceeds that of the simple lattices used here for illustration. However, principles of activation energies, processes of atomic motion, and the links among them still apply in anisotropic media under stress, that is, most minerals in rocks geologists investigate. The correspondence of activation energies presented in Figures 2.5 and 2.6 highlights this. Moreover, diffusion enhanced by deformation has been reported in metals and silicate minerals (Cohen, 1970; Büttner, 2005; Büttner and Kasemann, 2007; Reddy et al., 2006; Kramar et al., 2001; Reddy et al., 2001; Yund et al., 1981).

### 2.5.1 Metals

A variety of experiments in the 1950s and 1960s explored deformation enhancement of diffusion in metals (Brown and Blackburn, 1963; Fara and Balluffi, 1958; Lee and Maddin, 1961; Simmons and Dorn, 1958; Watanabe and Karashima, 1970), although results were often not conclusive (e.g. Ruoff and Balluffi, 1963b). Despite the lack of conclusive detection in that study, the models presented in companion papers indicate that there could be a small effect on diffusion from point defects and possibly a larger effect due to short-circuiting along dislocations and/or grain boundaries, particularly if line defects are mobile (Balluffi and Ruoff, 1963; Ruoff and Balluffi, 1963a).

### 2.5.2 Silicate Minerals

#### *Tourmaline*

Tourmaline commonly occurs as an accessory phase in evolved magmatic rocks and metapelites. Its growth zoning can record complex histories of metamorphism (e.g. van Hinsberg et al., 2011). Büttner (2005) and Büttner and Kasemann (2007) showed that deformation enhances element mobility across a growth zoning compositional boundary in tourmaline in a highly deformed pegmatite. Büttner (2005) showed major element mobility across growth zones proportional to the degree of grain deformation. Using high-resolution transmission electron microscopy, he determined that dislocation creep and subgrain rotation were the primary deformation mechanisms modifying growth zoning. Büttner and Kasemann (2007) extended this to trace elements and B-isotopes showing variable mobility enhancement. Unfortunately, diffusion coefficients are not available for tourmaline,

preventing a quantitative assessment of these observations.

### *Zircon*

Reddy et al. (2006) combined panchromatic and wavelength cathodoluminescence (CL), electron backscatter diffraction (EBSD), and ion microprobe analyses to demonstrate deformation-enhanced diffusion of rare earth elements (REEs) in zircon. The crystal analyzed was deformed at amphibolite facies ( $\sim 750^\circ\text{C}$ ) in a plagioclase high-strain zone about 2 mm-wide in a Miocene olivine gabbro collected near the Atlantis II Fracture Zone in the Indian Ocean. In one corner of the grain, CL and EBSD showed increasing crystallographic misorientation and low-angle subgrain boundaries accompanied by REE concentration profiles for which volume diffusion alone cannot account. For crystal age and temperature conditions (11 Mya and  $750^\circ\text{C}$ ), REEs should travel on the order of 1 nm. In the more deformed parts of the crystals, REE travelled approximately 50  $\mu\text{m}$ , in the same amount of time or less, an enhancement of four orders of magnitude. In addition, the authors saw in CL that primary magmatic zoning is increasingly homogenized in areas where misorientations are recorded by EBSD. The authors conclude that dislocation creep was the primary mechanism of deformation, which provided mobile, high-diffusivity pathways within the deforming region of the grain and enhanced bulk diffusion. Although uncertainties are not clearly reported, at least a qualitative link between deformation and diffusion can be drawn.

### *Muscovite*

By step-heating naturally deformed muscovite “fish” from a pegmatite vein in the Siviez-Mischabel Nappe in the western Swiss Alps, and measuring Ar loss using ultraviolet laser ablation, Kramar et al. (2001) tracked increasing argon loss with increasing deformation. More deformed regions of the grains give younger  $^{40}\text{Ar}/^{39}\text{Ar}$  ages. The least deformed regions of grains still preserve Variscan metamorphic ages, but these are lost in the more deformed regions. In particular, significantly younger ages appear primarily in shear bands.

### *Feldspar*

#### *Argon*

Argon is an important isotopic system for constraining thermal histories in feldspars as well

as micas. Reddy et al. (2001) explored the effect of deformation on  $^{40}\text{Ar}/^{39}\text{Ar}$  in three potassium feldspar clasts that underwent different amounts of deformation but share thermal history. The samples were collected from a Late Mesoproterozoic arkose on the Isle of Skye, Scotland, with clasts as old as Archean/Paleoproterozoic. Deformation microstructures of the clasts were determined with optical and scanning electron microscopy (SEM) and orientation contrast imaging. Atomic number contrast images on the SEM and ultraviolet laser microprobe were used for high spatial resolution measurements of Ar loss in all three clasts. Although intra-grain microstructure and age patterns are complicated, Reddy et al. (2001) conclude that increasing complexity in deformation microstructure correlates with Ar loss.

### *Oxygen*

Oxygen diffusion in feldspars plays a key role in metamorphic reactions. To test its potentially enhanced diffusion, Yund et al. (1981) used bulk  $\delta^{18}\text{O}$  analyses at 450°C and 750°C to investigate whether dislocations introduced by previous plastic deformation enhance oxygen diffusion in albite. These authors found enhancement of diffusion distance by five orders of magnitude over a dislocation radius of 4Å for experimentally deformed grains, but only about one order of magnitude change for a naturally deformed crystal despite it having higher dislocation density than the grains experimentally deformed. This showed that the effect of old damage is negligible compared to active deformation.

## 2.6 Implications of Deformation-Enhanced Diffusion

Present petrological tools used in minerals to determine pressure, temperature, time, and chemical conditions do not take into account the dependence of diffusion on deformation. Instead, they assume preservation of the desired information even after deformation. As previous papers have also pointed out (e.g. in the geochronologically central mineral zircon Reddy et al., 2006), the possibility that chemical robustness of deformed minerals is not satisfied has potentially severe implications for dating and geothermobarometry. However it also has a potential application in strain speedometry.

### 2.6.1 Geothermobarometry and Isotope Geochronology

The elemental and isotopic composition of minerals is used extensively to derive the physical and chemical conditions, and age, of their host rocks. The tools used for this all rely on the assumption that the mineral retains its composition and hence the information for the desired stage in its evolution. This assumption requires that diffusion has not destroyed this record. Closure temperature is defined as the lower temperature limit for static diffusion to be efficient on the timescales of interest, and is regarded as the temperature below which signals are preserved. Dodson (1973) developed an equation for this threshold temperature:

$$T_c = (E_{\text{ActD}}/R + 2T_c^1) \div \ln \left( \frac{AR(T_c^1)^2 D_0}{E_{\text{ActD}} s a^2} \right) \quad (2.4)$$

where  $T_c$  is the closure temperature,  $T_c^1$  is an estimated trial closure temperature to constrain  $T_c$ ,  $A$  is a geometric factor,  $s$  is the cooling rate, and  $a$  is the effective diffusion radius. As in preceding equations,  $E_{\text{ActD}}$  is the activation energy for diffusion,  $R$  is the universal gas constant, and  $D_0$  is the pre-exponential factor for the diffusion rate  $D$ .  $D$  is given for a particular absolute temperature.

This metric suggests that the information has been preserved, as long as the sought-after conditions occurred below the closure temperature. However, the  $D$  in Eq. 2.4 is the static diffusion coefficient, which we have argued will temporarily be elevated during deformation. This effectively lowers closure temperatures in deformed crystals (e.g. Reddy et al., 2001). Moreover, the effect on each element varies depending on its activation energy for diffusion. As such, the effect on fast-diffusing elements such as Ar and Li should be much higher than on slow diffusing elements such as the rare earth elements (Figs. 2.5 and 2.6). We therefore predict that, on first-order approximation, the Ar isotopic dating system should be affected first and most by deformation, followed in order by Rb-Sr, U-Pb, and Nd-Sm. Also, in general, thermobarometers based on major elements should be less affected than thermobarometers based on trace elements.

### 2.6.2 Strain Speedometry

Geologists often study deformed rocks, and untangling deformation history amidst thermal and barometric complexity is their goal. The link between deformation and diffusion could provide a missing piece of evidence: time. Quantification of deformation-enhanced element mobility may

provide a time-dependent, measurable tool to structural geologists to be able to estimate strain rate at a mineral-scale, which is currently impossible for rock-forming minerals.

To measurably connect bulk deformation and intra-crystalline diffusion, a simultaneous physical and chemical marker must be present in a mineral that records the bulk history of the rock. The ideal marker (for both strain and diffusion measurements) must be one whose initial geometry and elemental concentration pattern can be measured or inferred with a high degree of confidence. This could be on a very small scale (e.g. deformed and undeformed parts of a single crystal), or on a large scale (where a single lithology expresses different degrees of deformation). Compositional growth zoning can serve as such a marker, as illustrated with tourmaline (Section 2.5.2; Büttner, 2005). (Tourmaline, however, is not widely useful for a bulk rock strain speedometer since it usually occurs as an accessory phase with different rheology than its host rock.)

### Element Concentration Profiles

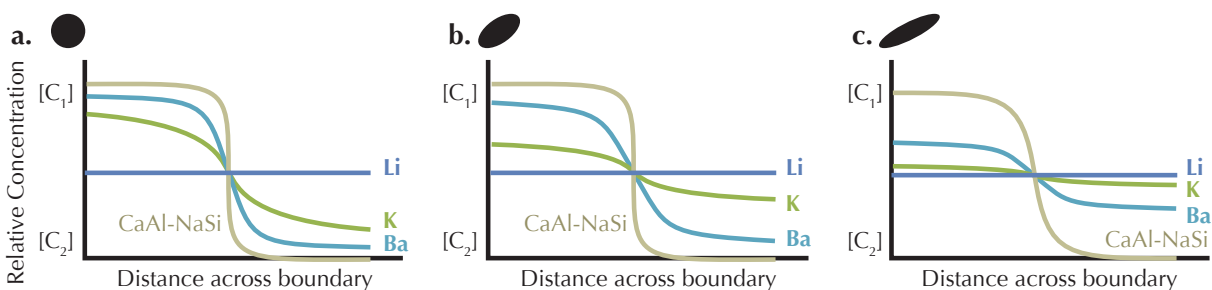


**Figure 2.7** Concentration profiles measured across a compositional boundary in an undeformed case (a.), at intermediate strain (b.), and at the highest strain (c.). Elements with different activation energies are differentially affected by strain: slower moving elements with high activation energies for diffusion may not show any change in their diffusion profile until the highest strain (CaAl-NaSi interdiffusion). Fast-moving elements such as Li may show no change because their initial profile had no contrast.

Composition profiles measured across the compositional zoning boundaries in equivalent areas of the crystals in undeformed and deformed regions or crystals provide the key to assessing the link between deformation and diffusion. At the time of crystallization, the growth zone boundary is a sharp step. Over time, the boundary is smoothed due to diffusion of atoms down the chemical gradient (Fig. 2.7a). Accepting that deformation enhances diffusion, with increasing strain, the slope of the profile across the boundary becomes more smooth (Fig. 2.7b and c). By fitting the diffusion profiles for the different elements, we can quantify the change in diffusivity for each element

resulting from deformation and from that the energy contributed by strain.

To fit the diffusion profiles, we use the diffusion couple equation (Zhang, 2010). One growth zone has concentration  $C_1$ , the other  $C_2$ . The concentration  $C$  along the distance  $x$  measured perpendicular to the boundary is then given by

$$C = \frac{C_1 + C_2}{2} + \frac{C_1 - C_2}{2} \left( \operatorname{erf} \left( \frac{x}{\sqrt{4Dt}} \right) \right). \quad (2.5)$$

where  $D$  is the static diffusion rate (in  $m^2/s$ ) and  $t$  is the apparent duration of deformation (in  $s$ ).

The duration of diffusion has been the same for all elements and can be estimated from the slowest diffusing element (i.e. the element least affected by deformation-enhanced element mobility). Using this time, we can calculate the deformation-enhanced diffusivity for the other elements by re-arranging the modelled concentrations and solving for  $D$ :

$$D = \frac{1}{4t} \left( \frac{x}{\operatorname{erf}^{-1} \left( \frac{2C - C_1 + C_2}{C_1 - C_2} \right)} \right)^2. \quad (2.6)$$

The enhancement of diffusivity depends on the element because different elements should be accelerated differently (but predictably) because of their different activation energies, with an element with a low  $E_{\text{ActD}}$  most affected.

### ***Activation Energy Contributions from Strain***

With an energy grant from strain ( $E_{\text{strain}}$ ), an atom needs less energy ( $E_{\text{strain-reduced}}$ ) to achieve the energy goal for diffusion ( $E_{\text{ActD}}$ ). That is:

$$E_{\text{strain-reduced}} = E_{\text{ActD}} - E_{\text{strain}} \quad (2.7)$$

Given strain-reduced activation energies for a suite of trace elements, a relationship can be determined between the calculated  $E_{\text{strain-reduced}}$  and the corresponding published activation energy values for diffusion ( $E_{\text{ActD}}$ ). We expect the curve to be a line with slope = 1 and intercept at the energy contribution from strain ( $E_{\text{strain}}$ ). This is directly proportional to the activation energy for the deformation mechanism at work to mobilize the atoms since it is based on the extent to which atoms move more easily. Within a grain, assuming that stress is constant over the crystal size- and

diffusion time-scales,

$$\dot{\epsilon} \propto \exp(-E_{\text{ActM}})$$

from Eq. 2.3. The quantity  $E_{\text{ActM}}$  can be considered the activation energy required to reach a situation in which strain can contribute energy and therefore reduce the atom contribution. Thus,

$$\dot{\epsilon} \propto \exp(-E_{\text{strain-reduced}}).$$

For slow-diffusing species,  $E_{\text{ActD}}$  and  $E_{\text{strain-reduced}}$  will not differ significantly except at high strain and strain rate. However, fast-diffusing species will be more affected. Figure 2.7 illustrates this affect. If elements diffuse very rapidly, like Li, then they will not be useful for this analysis. All elements are eventually accelerated by strain, but the faster diffusing species (e.g. K and Ba in feldspar) can go distances of tens of microns. Slowly diffusing species (e.g. major elements involved in interdiffusion in feldspar) may travel the same percentage farther as the faster diffusing species but only go a matter of angstroms. Until analytical capabilities are more refined, only the effect on the faster diffusing species is measurable.

### *Measuring Strain*

In order to fully determine bulk rock strain rate from the minerals analyzed, not just the duration of deformation but also the individual grain-scale strain and its relation to bulk rock strain must be measured.

Methods for quantifying strain have been developed across a range of scales from kilometers to sub-grain scales (e.g. Ramsay and Huber, 1983; Lisle, 1985; Bhattacharyya and Hudleston, 2001; Mookerjee and Peek, 2014). Strain is usually measured as linear or angular change, which represents just one dimension of three-dimensional deformation. It is not necessary to quantitatively measure the full three-dimensional strain field, as long as the one-dimensional strain measurement can be made in a dimension that corresponds to the diffusion measurement. We offer an example of this in Chapter 4.

## 2.7 Conclusion

Diffusion and deformation in crystal lattices are both processes of element mobility but under different driving forces. Individually, they have different results. Diffusion accomplishes a homogenous distribution of elements with no long-range shape change while deformation achieves a measurable shape change. Yet they are linked at their most basic level: activation energy. We have argued from first principles that when deformation proceeds along with diffusion, it enhances the mobility of all elements, whether major constituents of the crystal lattice or impurity ions. This link is not new; still, the fields of petrology and structural geology have viewed diffusion and deformation from different perspectives despite the similarity and connection between the processes. This geology-based, first principles documentation of strain-enhanced diffusion calls into question the basic assumptions of several geologic tools. If used in deformed rocks, the requirements for present geothermobarometers and geochronometers are not met: diffusion is not static. Conditions of pressure, temperature, and time are not simply frozen into deforming minerals, and these tools must be re-evaluated for use in deformed settings. However, linking these processes connects deformation to a time-dependent process with measurable results, potentially allowing structural geologists to infer the otherwise elusive strain rate from the rock record.

## CHAPTER 3

---

### From Theory to Practical Application

---

In Chapter 2, I show that diffusion and deformation are both processes of atomic migration which are linked by the energy barrier to motion. Strain can contribute elastic energy to bonds, thus reducing the energy needed to break the bonds and enhancing element mobility. If this energy discount is enough to expedite diffusion over geologic timescales, likely aided by additional enhancements by traveling diffusion highways such as dislocations, the effect should be measurable. It is (Büttner and Kasemann, 2007; Reddy et al., 2006; Yund et al., 1981). This effect should also have an impact on geochronometers and geothermobarometers. Geochronometers have been reset and otherwise disrupted (Kramar et al., 2001; Reddy et al., 2001). One under-explored implication of strain-enhanced diffusion exploits the time-dependent process of diffusion to develop a strain speedometer. I laid the theoretical basis for a method to infer an approximate strain rate in Chapter 2. In Chapter 4 I put the theoretical model to the test to evaluate whether strain enhanced diffusion in naturally and variably deformed, compositionally zoned plagioclase phenocrysts with the goal of creating a plagioclase-based strain speedometer that can be applied in a variety of deformational settings and lithologies.

---

Can We Measure Deformation-Enhanced Element Mobility in  
Naturally-Deformed Plagioclase?

---

Naomi Barshi, Christie Rowe, and Vincent van Hinsberg

## 4.1 Introduction

Geologists use a variety of tools to detangle histories of temperature, pressure, and chemistry. These thermobarometers and geochronometers are based on temperature- and pressure-dependence of element mobilities between and within minerals, but do not account for systematic enhancement of element mobility by deformation (e.g. Hodges, 1991). We have evaluated the possible influence of deformation on element mobilities and have shown from first principles that deformation can measurably enhance element mobilities, hence static-diffusion-based thermobarometers and geochronometers may be compromised in deformed rocks (Chapter 2). However, linking deformation and diffusion provides a missing term in the current toolkit used to measure parameters of deformation: time. In this chapter, we present the first detailed study seeking to document deformation-enhanced element mobility in plagioclase, a rheologically and modally dominant mineral in Earth's crust and a key mineral in geochronometers and thermobarometers (Spear, 1993; Platt and Behr, 2011; Rybacki

and Dresen, 2004, and references therein). If deformation-enhanced element mobility is measurable, geochronometers and thermobarometers in plagioclase must be re-evaluated while a new tool can be developed to infer bulk-rock strain rate in crustal shear zones.

## 4.2 Approach

Measuring deformation-enhanced element mobility requires a simultaneous physical and chemical strain marker that records changes across a complete strain spectrum. We measured changes in chemistry with increasing strain in growth-zoned plagioclase phenocrysts from a natural strain gradient. We characterized this strain gradient in the field, known from the literature to have a gradient in deformation fabrics in an otherwise homogeneous rock body, the San José pluton in the Peninsular Ranges Batholith of Baja California, México (e.g. Johnson et al., 2004; Vernon et al., 2004, Johnson, pers. comm. 2013). Field methods and observations are discussed in more detail in Section 4.3, but their primary aim was to establish the deformation characteristics from which to isolate samples for chemical analyses and later reconnect them to their field context.

### 4.2.1 Chemical Analytical Methods

Deformation-enhanced element mobility should be measurable as a systematic change in chemistry with increasing strain given a compositional disequilibrium or gradient. Primary growth-zone boundaries in plagioclase phenocrysts are ideal locations to measure deformation effects. These compositional differences, formed during growth, are not in equilibrium and hence produce a chemical gradient that drives diffusional re-equilibration across the zone boundary. The starting composition contrast is known from other grains or from undeformed regions within a heterogeneously deformed single grain, which makes it possible to track the differential diffusional re-equilibration for variably deformed (parts of) plagioclase grains by measuring transects across this boundary. In all cases, we measured en-echelon lines of points traversing primary zoning boundaries in variably deformed plagioclase grains.

We measured Na, Ca, Al, Si, K, Fe, and Mg *in situ* using the JEOL 8900 Superprobe at McGill University by wavelength dispersive spectroscopy (WDS) line scans. Lines were run with a 15 kV accelerating voltage and 10 nA beam current. Line scans ranged in length depending on the geometry

of the phenocryst analyzed, but all were set to 5  $\mu\text{m}$  beam size (to limit sodium loss) and 5  $\mu\text{m}$  step size to avoid overlapping points. We also used WDS element maps to gain higher resolution images of major element concentrations. Map points had dwell times between 80 and 100 milliseconds under a focused beam at 15kV, 50nA, moving in 0.8  $\mu\text{m}$  steps, the highest achievable resolution.

Minor and trace elements were determined by Laser Ablation Inductively Coupled Plasma Mass Spectrometry (LA-ICP-MS). We analyzed *In situ* lines of points on the 193 nm Excimer ArF laser ablation system connected to a Nu Instruments micromass ICP-MS at Géotop/Université du Québec à Montréal (UQÀM), with an effective beam size of about 15  $\mu\text{m}$ . After testing if concentrations were sufficiently high above background, we analyzed for Li, Mg, K, Ca (as internal reference to electron microprobe measurements), Sr, Ba, Ce, Eu, and Pb, calibrated against NIST 610 with a frequency of 15 Hz and fluence of 9 J/cm<sup>2</sup>.

In addition to major, minor, and trace element analyses in plagioclase phenocrysts, we used the Holland and Blundy (1994) thermobarometer on pairs of hornblende and plagioclase grains in samples distributed from the interior of the northern unit to the edge of the NW pluton to test for resetting of pressure-temperature information. Concentrations of Na, K, Ca, Fe, Al, Ti, Si, and Mg were measured using the JEOL 8900 Superprobe at McGill University. Apparently unaltered pairs of adjacent plagioclase and hornblende phenocrysts were selected for thermobarometry. In samples we determined had undergone bulk deformation, we included plagioclase grains which showed signs of internal deformation such as curved twins. Since such grains were rare, we considered them along with grains which underwent no apparent internal deformation.

## 4.3 Field-Scale Studies

### 4.3.1 Geologic Setting

We investigated the carapace of the Cretaceous San José pluton, Peninsular Ranges Batholith, Baja California, México. The San José pluton is a late, tonalitic nested pluton stitching a suture between an island arc and North America (e.g. Murray, 1978; Johnson et al., 1999). The amphibolite facies Alisitos Arc is the country rock for this pluton (Figure 4.1; e.g. Johnson et al., 1999; Alsleben et al., 2008; Wetmore et al., 2002). The Mártir Thrust separates Alisitos rocks of arc affinity from rocks with continental detrital components and has been interpreted as a major suture zone (Johnson

et al., 1999). The Mártir Thrust is located northeast of the San José pluton and was active 115 Ma - 108 Ma (Johnson et al., 1999), during the closing of an ocean basin (Wetmore et al., 2002). After the ocean basin closed and fault activity ceased, plutons intruded the suture zone at mid-crustal levels with no major solid state deformation after emplacement (e.g. Johnson et al., 2008), although internal deformation structures are present, interpreted as emplacement-related (see below).

Regional exhumation studies indicate a sharp gradient in cooling ages in this part of the Peninsular Ranges Batholith, sandwiched between the Main Mártir Thrust and the Rosarito fault (a younger fault several kilometers to the southwest of the San José pluton), in the western portion of the doubly-vergent fan structure of the Sierra San Pedro Mártir, a large mountain range immediately east of the San José pluton (Schmidt et al., 2009). Schmidt et al. (2009) integrated cooling ages from  $^{40}\text{Ar}/^{39}\text{Ar}$  in K-feldspar and biotite, apatite fission tracks, U-Pb zircon ages, and Al in hornblende thermobarometry to constrain exhumation history. They suggest that maximum crustal thickness was 55 km in the east and that the region cooled rapidly with exhumation initiating around 100 Ma, migrating eastward to be mostly complete by 85 Ma with continued denudation into the Paleogene.

Murray (1978) used texture and mineralogy to define a nested series of three intrusive units within the San José pluton with gradational contacts: the southern, central, and northern units (Fig. 4.1). The northern unit has an outer carapace about 0.5-1.5 km-wide of biotite-defined, contact-parallel, foliation that increases in intensity toward the pluton's edge. The development of foliation in this "marginal outer unit" (Murray, 1978) likely occurred as the result of the intrusion of the southern and central units into a partially-cooled northern unit in the intervening 4.4 Myr between intrusive pulses (Johnson et al., 1999, 2004; Vernon et al., 2004). There is no evidence for deformation after emplacement of the central unit around  $103.4 \pm 1.0$  Ma (Johnson et al., 1999). The northern unit mineralogy is about 65 modal percent plagioclase, 10% hornblende, 8% biotite, 15% quartz, and less than 2% accessory phases (Murray, 1978; Johnson et al., 2003, this study).

Aluminum-in-hornblende barometry combined with the wet tonalite solidus peg the emplacement and deformation conditions at depth at  $\sim 680^\circ\text{C}$  and 300 MPa (7-12 km; Vernon et al., 2004). Post-emplacement deformation and alteration were minimal: white mica filling intra-granular fractures in plagioclase phenocrysts suggests that water was present during or after brittle deformation post-dating pluton emplacement (Johnson et al., 2003; Vernon et al., 2004).

The relative simplicity of stress, strain, time, and temperature history make the San José pluton

an ideal natural laboratory in which to test the hypothesis that strain enhances element mobility in a rheologically dominant mineral.

#### 4.3.2 Evolution from Magmatic to Gneissic Fabric

We sampled two transects, each from undeformed tonalite containing only magmatic fabric to strongly foliated gneissic tonalite (Figs. 4.1 and 4.2). Johnson et al. (2003)'s "marginal unit" of the San José pluton shows a complete, almost continuously exposed evolution from abundant euhedral plagioclase and hornblende phenocrysts in poorly- to well-developed magmatic fabric to a texture containing flattened biotite in an interconnected, planar manner that resembles gneissic foliation. We detail this transition in the following sections to support the interpretation of fabric overprint.

##### *Starting Materials: Undeformed Rocks and General Descriptions*

Undeformed San José tonalite in the northern unit is phaneritic, with varying alignment of minerals from apparently random distribution near the center of the northern unit (e.g. MX23 in Figure 4.1, a. in Figure 4.2) to linear alignment of elongate hornblende and plagioclase phenocrysts several hundred meters closer to the pluton's edge. The primary minerals are plagioclase (65 - 75 mode %), hornblende (15 - 25%), biotite (5%), and quartz ( $\leq 15\%$ ), with minor accessory phases including titanite.

**Plagioclase** has three habits in the northern unit, which change in abundance with deformation (Fig. 4.2): growth-zoned phenocrysts, twinned rectangular grains, and equant, anhedral groundmass grains. Phenocrysts in undeformed rocks are visibly zoned and euhedral, usually 2.5x4 mm but  $\leq 6$  mm, with centers slightly more yellow in (hand sample and outcrop) than their white outer rings. Large, zoned phenocrysts account for about 15% of the plagioclase in the undeformed rocks, and decrease in abundance and slightly in size toward the edge of the pluton. In isotropic and weakly foliated rocks, phenocrysts comprise about 60% by field-estimated mode percent (all modal field estimates  $\pm 5\%$ ). Crystals that are blockier and more translucent than the phenocrysts, described here as "twinned rectangular grains", are often twinned and striated. Typically they are about 2-3mm long and 1.5-2mm wide and account for at least 20% of the plagioclase in undeformed rocks. Matrix/Groundmass plagioclase crystals in this phaneritic tonalite are typically about 1mm or smaller. Their abundance increases toward the edge of the pluton from about 20% in undeformed

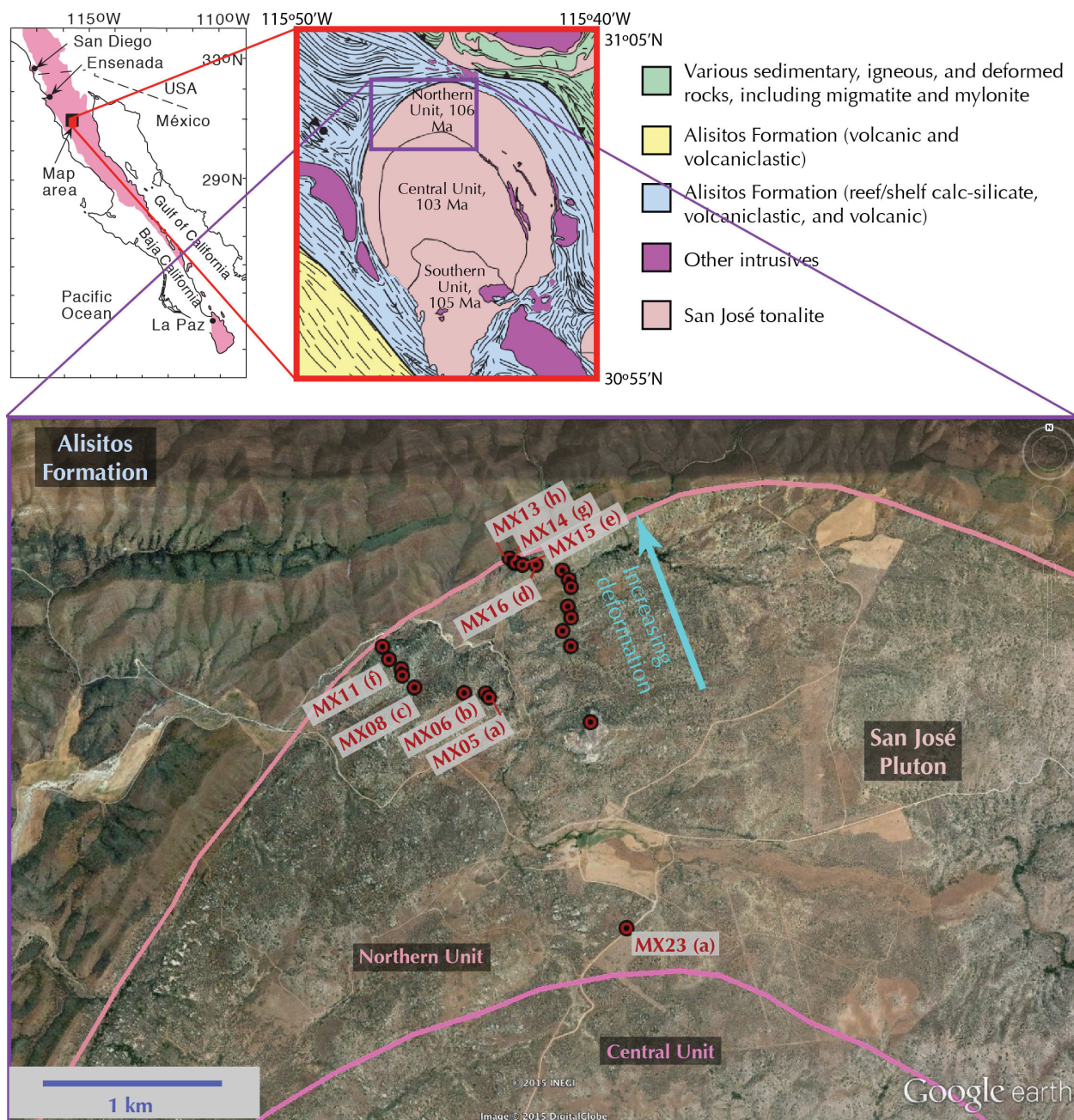


**Figure 4.1** The Lower Cretaceous San José pluton is located in the Peninsular Ranges Batholith, northern Baja California, México. Oriented samples were taken in the outer and oldest unit of the San José pluton, which experienced solid-state deformation during nested pluton emplacements Johnson et al. (1999). Samples were taken along two transects of the outer margin of the pluton from undeformed to the most deformed edge of the pluton. Letters following sample names refer field-identified strain increments illustrated in Figure 4.2. Overview maps modified from Johnson et al. (1999), satellite image from GoogleEarth.

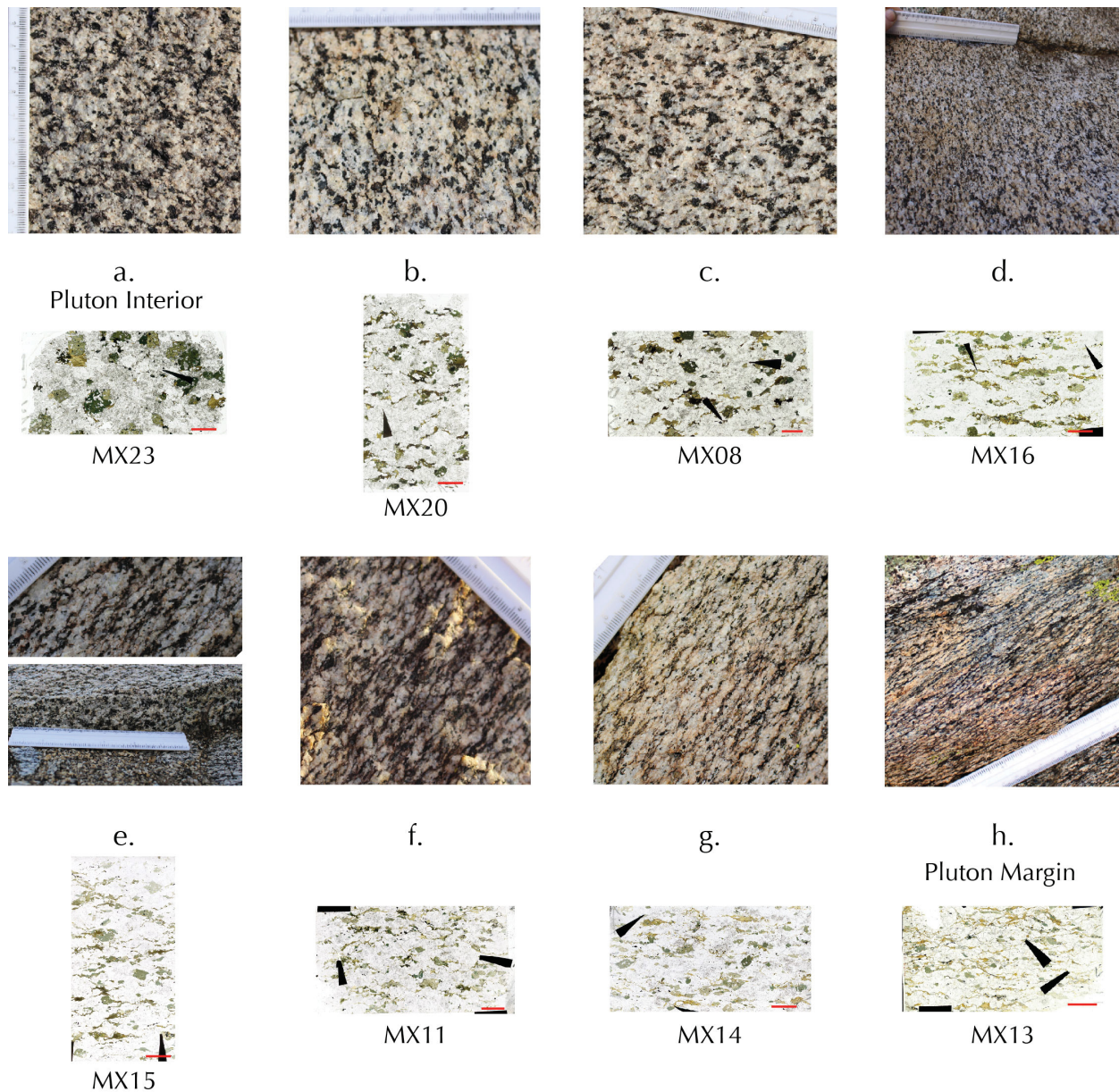


**Figure 4.2** From the interior to the edge of the pluton, mineralogy, shape, size, and geometry of the San José tonalite evolves from magmatic fabric to gneissic foliation. Top: outcrop photos taken with 15-cm long ruler, divisions shown in mm. Photos oriented such that the upper left corner is up and northwest. Bottom: thin sections scanned in plain polarized light with all scale bars 5mm. Photos are oriented with foliation/preferred mineral alignment (if present) horizontal and parallel to the thin section cut (XZ sections). Black arrows point to phenocrysts selected for chemical analyses. See text for full description.

and slightly deformed rocks.

**Hornblende** is stubby-prismatic in undeformed rocks. In the interior edge of the northern unit, hornblende grains about 3-4 mm are randomly oriented (Fig. 4.2a). Closer to the carapace, hornblende occurs as more elongate crystals which share a linear alignment (Fig. 4.2b-e) that persists until flattened, interconnected biotite dominates the mafic phases and defines a foliation that resembles gneiss (Fig. 4.2f-h). Proportion of hornblende in undeformed rocks varies from 15% to as much as 25%.

**Biotite** is rare in undeformed portions of the pluton, but where present forms euhedral books of 1-2mm, up to 3mm with only about 5% field-estimated mode (Fig. 4.2). Toward the edge of the pluton, it increases in abundance at the expense of hornblende and appears to become more brown-green in colour.

**Quartz** accounts for less than 15% of the rock and is reduced in grain size toward the edge of the pluton to the point that it is indistinguishable from plagioclase in outcrops close to the edge of the pluton. Where visible, it is of the same shape and size as the matrix plagioclase, though grey to smoky purple.

### *Characterizing Field-Scale Changes*

In the field, we defined a set of criteria marking changes in mineral modes, plagioclase phenocryst abundance, mineral alignments, and overall rock texture illustrated in Figure 4.2.

- a. Undeformed with little to no preferential alignment of minerals with abundant, euhedral hornblende and plagioclase phenocrysts
- b. Weak to linear alignment of elongated hornblende and plagioclase phenocrysts
- c. Appearance of flattened, elongated wisps of biotite
- d. Increasing mineral alignment and increasing biotite abundance
- e. Both what we interpret to be magmatic and flattening textures visible with aligned long axes of magmatic minerals with increasingly flattened biotite starting to surround plagioclase phenocrysts

- 
- f. Biotite becomes increasingly connected, abundant, and flattened into an intermediate level of flattening foliation
  - g. Less abundant plagioclase phenocrysts and nearly no hornblende of any size in well-developed flattening foliation
  - h. Most deformed state at the pluton's northwestern margin with fully developed, biotite-defined foliation, and rare phenocrysts of either hornblende or plagioclase

#### *First Hints of Deformation: Biotite Alignment*

In outcrops sampled nearer the interior of the northern unit, biotite folia have no visible preferred alignment but become more aligned and flattened toward the pluton's edge (Fig. 4.2). The first indication of change in biotite shape is as elongate wisp-like "stringers" (Fig. 4.2c).

Alignment of these biotite wisps is similar among outcrops (Fig. 4.3). Strikes are mostly in the range 060-070 with steep dips, usually  $\geq 80^\circ$  S (occasionally N), parallel to the pluton-wall rock contact. A fabric similar to that in Figure 4.2c persists for several hundred meters along the transects we walked until it gives way or turns into a strong preferential alignment of strongly flattened biotite. Hornblende alignment and abundance also changes (Fig. 4.3).

#### *Oblique Hornblende and Biotite Alignments*

In the least deformed rocks, there is no apparent alignment of biotite, so there is no divergence between hornblende and biotite alignments. In the rocks sampled at intermediately points along the transects, elongated biotite alignment measurably differs from hornblende alignment over hundreds of meters across strike (Figs. 4.3 and 4.4). Field measurements from several outcrops between about 670 and 300 m away from the pluton's NW edge indicate hornblende long axes are aligned within the average plane 250, 82 NW while biotite lies in the average plane 045, 90. The difference in strike is  $25^\circ$  and  $8^\circ$  dip. Biotite measurements are of the biotite wisps described above which increasingly share the average alignment.

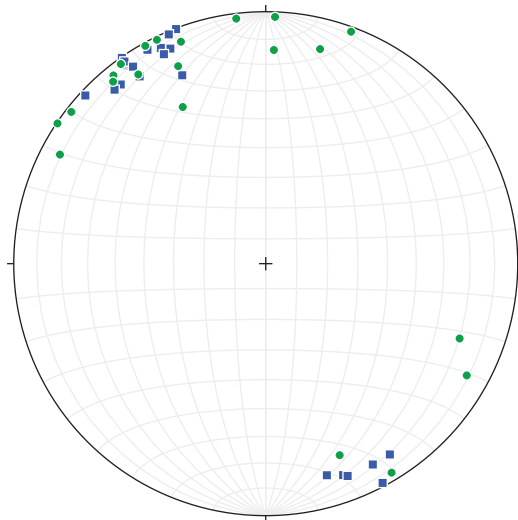


**Figure 4.3** Lower hemisphere equal area stereographic plot of poles to planes containing biotite and hornblende alignments from the first appearance of biotite wisps until biotite and hornblende alignments converge. In general, hornblende alignments (blue squares) show less scatter than biotite wisp alignments (green circles, Fig. 4.2c).

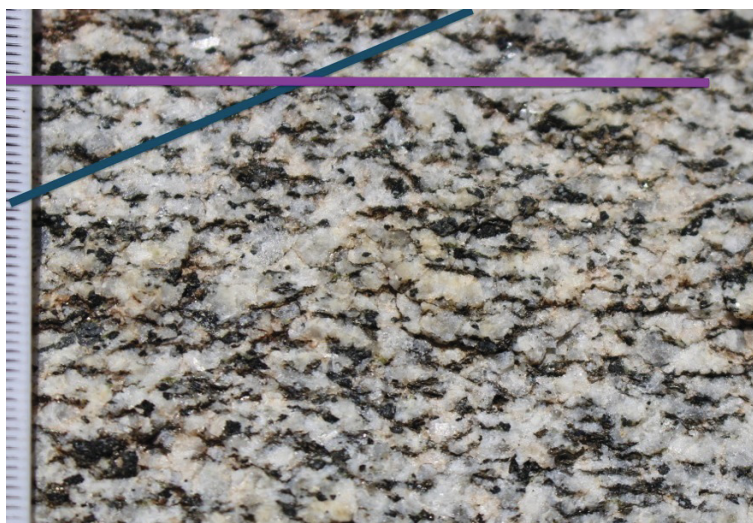


**Figure 4.4** Two orientations of biotite and hornblende varying in rake between  $20^\circ$  and  $45^\circ$ . Scale division in mm.

---

*Magmatic and Secondary Fabrics Both Visible*

At intermediate points along our transects from northern unit interior to edge, the magmatic minerals are still visible but become increasingly aligned. In particular, the twinned rectangular plagioclase grains become more aligned based on cleavage/twin orientations noted in the field. Biotite becomes flatter and more abundant. Figure 4.2d and 4.2e illustrate this development. As shown in Figure 4.4, the apparently over-printing fabric of aligned minerals is regularly spaced.

*Bulk Flattening and Alignment of All Minerals*

Closer to the edge of the pluton, more of the minerals are more strongly aligned, with flat, increasingly connected biotite grains and fewer large phenocrysts of both plagioclase and hornblende. This is particularly visible in thin sections (Fig. 4.2e-f) which have markedly more aligned, generally smaller grains and more biotite than do samples taken farther from the pluton's edge (compare Fig. 4.2e and a).

*Pervasive Planar Alignment of Minerals*

Nearest the pluton's edge, a preferential alignment of platy biotite and general alignment of all minerals pervades (Fig. 4.2), with interconnected, platy biotite fully surrounding plagioclase grains that mostly fall in either the groundmass or small phenocryst categories outlined above. At the edge of the pluton, it is flattened into  $\leq 6$ mm diameter pancakes which define the  $\sim 3$  mm-spaced foliation. Hornblende is very rare and very small when present. Biotite dominates the mafic phases.

These field-scale observations are supported by microstructural observations of the same first-order changes in mineralogy and mineral shapes. Quartz increasingly displays undulose extinction and grain size reduction probably by subgrain rotation and grain boundary migration recrystallization (Stipp et al., 2002). In intermediately deformed samples, at locations where hornblende and biotite begin to rotate into parallelism, quartz is concentrated into high aspect ratio areas in thin section which have not quite achieved quartz ribbon status. In the most deformed samples, quartz is milled into micron-sized grains in micro-shear zones with similarly sized plagioclase grains and long, thin biotite. In these samples, some plagioclase also has minor undulose extinction. In outcrop and in thin section, the visibility of plagioclase zoning generally decreases. Hornblende shrinks from

several-millimeter long, inclusion-rich grains to small lozenge-shaped grains often surrounded by or edged by elongated biotite. Thin-section and sample-scale microstructural evidence allowed us to characterize these changes quantitatively using image analyses.

## 4.4 Sample-Scale Studies

A subset of samples taken in the field were used for structural analyses on hand-sample and thin section-scales. A brief description of these samples is given in Figure 4.5 with microstructural observations detailed in Figure 4.6.

### 4.4.1 Quantitative Methods

Plagioclase dominates the mode of these rocks, and we therefore measured changes in plagioclase grain shape parameters to infer bulk rock strain in whole thin section scans of samples taken across collection transects. We measured plagioclase phenocryst shape, size, abundance, and orientation. We conducted the same image analyses on the mafic phases (biotite and hornblende) to assess the shape changes in these less common and weaker phases, which we noted contributed changes to bulk rock appearance at the field scale. Because plagioclase phenocrysts may act as active markers which do not represent whole-rock deformation we needed to characterize the contribution of changes in shape in minor and weaker phases. Thin sections used for image analysis were cut parallel to lineations and perpendicular to foliations (XZ-section) for maximum structural information. Images were exported such that the most common apparent alignment of mineral long axes were approximately horizontal.

### *Digitizing Mineral Grains*

Each thin section was scanned whole in plain- and cross-polarized light at a minimum resolution of 1200 dpi.

All plagioclase phenocryst grain boundaries were outlined in Adobe Illustrator directly on thin section scans with the aid of an optical microscope. Phenocrysts were circled in two confidence classes based on sureness of grain boundary locations. Grains whose boundaries were clear, not inter-grown or indistinguishable from twin boundaries, were considered highest confidence. Low

Sample Name	Distance from NW pluton edge (m)	Field Strain Classification	Orientation of Important Features	General Description
MX23	2170	Undeformed (a)	None measured	Reference sample from interior of northern unit with no discernible preferred mineral alignments. Hornblende is main mafic phase. All grains are euhedral.
MX05	710	Undeformed (a)	None measured	Some preferential alignment of long axes of hornblende. Plagioclase and hornblende phenocrysts abundant with field-estimated mineral modes 70% Plg, 25% Hbl, 4% Bio, $\leq$ % Qtz
MX06	670	Biotite wisps (b)	Biotite stringers and hornblende alignment in plane ~063, 81 S	Similar to MX05, except Hbl more patchy and smaller. Hbl and Bio long axes generally parallel
MX20	360	Biotite wisps (b)	Hbl long axes in plane ~250, 80 NW; Bio long axes in plane ~215, 75 NW	Field estimate that 20-30% of Plg long axes aligned with main mineral alignment with secondary alignment of elongate Bio wisps
MX08	340	Mafic phases at high angles (c)	Plane containing mafic phases ~50, 85 SE, but angle between them 10 - 45°	Still primarily apparently magmatic alignment of minerals with elongate Hbl but first indication of angular difference between Hbl and Bio alignments
MX16	90	Magmatic and Overprinted textures both visible (d)	Hbl in plane ~065, 86 SE. Bio in plane ~040, 79 SE. Divergence between Hbl and Bio: rakes ~25 - 30°	Prismatic Hbl also with overprinting Bio connected planar fabric spaced about 2-4 mm. ~50% of Plg phenocrysts with long axes aligned.
MX15	50	General flattening and alignment of all minerals (e)	General flattening into plane ~241, 79 NW	Hbl with high aspect ratio (sub-acicular) but predominant texture is overprinting, flattening and alignment of all minerals
MX11	70	Pervasive planar alignment biotite and most minerals (f)	Mineral alignments in plane ~228, 86 NW	Fewer large Plg phenocrysts noted than elsewhere in less deformed rocks. Bio found as round "pancakes" 4-5mm in diameter. (taken on southern transect where spacing of features differs from northern transect.)
MX14	30	Pervasive planar alignment biotite and all minerals (g)	Pervasive planar alignment of minerals ~233, 72	Hbl in sub-prismatic flakes mostly ~1.5x3 mm mostly aligned with Bio flattening fabric. Plg phenocrysts are rare (<1% of Plg) with most Plg grains ~1-2 mm.
MX13	1	Flattened, grain size-reduced, with closely-spaced biotite-defined flattening fabric (h)	Closely-spaced Bio-defined planar alignment of all minerals ~242,70 NW	Sample taken closest to pluton edge which displays highest degree of Bio flattening, connectivity, smallest spacing between planar Bio fabric, greatest field-apparent grain-size reduction, and very rare phenocrysts. Modal estimates: 65-70 % Plg, 25-30% Bio, with no Qtz noted in the field.

Figure 4.5 Field-based sample descriptions keyed to Figure 4.2.

4 Can We Measure Deformation-Enhanced Element Mobility in Naturally-Deformed Plagioclase?

Sample Name	Distance from NW pluton edge (m)	Field Strain Classification	Descriptions from Thin Sections (XZ-Sections)
MX23	2170	Undeformed (a)	Large, equant Hbl often with Plg inclusions 10% mode but only ~6 crystals/thin section. Rarely Bio clings to Hbl edges. Plg mostly as large, elongate phenocrysts with rare alteration to calcic centers but generally only apparently non-magmatic texture is fracture.
MX05	710	Undeformed (a)	Plg mostly as elongate phenocrysts (2-5 x 0.9-2 mm) with general long-axis alignment as noted in the field (at angle ~20° to base of thin section). Twinned rectangular and matrix Plg ~5 mode %. Hbl large and equant, 1.5 - 4mm diameter. Qtz interstitial without clear grain shapes.
MX06	670	Biotite wisps (b)	Very similar to MX05, also with sharp grain boundaries, elongated phenocrysts that share a weak preferred alignment.
MX20	360	Biotite wisps (b)	Plg still mostly large phenocrysts with slight increase of smaller grains (matrix and rectangular twinned Plg comprise ~5 mode %). Bio usually anhedral and blocky but sometimes with higher aspect ratio.
MX08	340	Mafic phases at high angles (c)	Abundant, large, visibly growth-zoned Plg phenocrysts. Qtz is often ≥ 1mm and had undulose extinction. Similar proportion of rectangular and matrix Plg (5%). Hbl in large, equant, poorly distributed phenocrysts. Bio has more internally foliated, book-like look.
MX16	90	Magmatic and Overprinted textures both visible (d)	Hbl with long fractures exploiting cleavage. Plg shows multiple twins more commonly than albite twins. Plg boundaries are usually sharp but sometimes have Bio growing off in “beards”. Hbl generally larger than Plg. Qtz had undulose extinction and some lobate edges. Much more distinct connectivity of Bio, alignment of phenocryst long axes, weakly aggregated Qtz than previous samples.
MX15	50	General flattening and alignment of all minerals (e)	Bio rarely wraps around Plg and Hbl phenocrysts. Bio more abundant than in MX16 at expense of both Hbl and Plg. Astoundingly more similar Plg long-axis alignment than previous samples with many grains ≥ 3x5 (up to 8) mm.
MX11	70	Pervasive planar alignment biotite and most minerals (f)	Plg shows albite twins and deformation twins and rare alteration of phenocryst centers and some patch zoning. Greater geometric inter-grain complexity than in previous samples. Hbl still ~12 mode % but more distributed and finer grained than previous samples. Some Qtz in elongated aggregates.
MX14	30	Pervasive planar alignment biotite and all minerals (g)	Qtz boundaries more lobate than previous samples and appear recrystallized in places. Plg displays more μm-scale fractures filled with white mica which are en echelon within grains but have no apparent pattern between grains. More than 50% of Plg phenocrysts have visible zoning preserved. Bio wraps around Plg phenocrysts.
MX13	1	Flattened, grain size-reduced, with closely-spaced biotite-defined flattening fabric (h)	Abundant micro-shear zones of recrystallized, 10-μm-scale Qtz with minor Plg. Bio is of a similar length but extremely high aspect ratio and anastomoses around (rare) phenocrysts. Some Plg phenocrysts are not visibly growth-zoned when expected to be growth-zoned based on similarity to other samples. Plg with deformation twins and straight to sub-lobate edges, especially when sided by microshear zones with minor undulose extinction and possible subgrains. Hbl present but in much smaller (10s of μm long). Instead of bent Plg grains as found in other samples, elongate Plg phenocrysts in this sample are often fractured and filled by Qtz and potentially alteration minerals such as white mica.

Figure 4.6 Microstructural descriptions keyed to Figure 4.2.

confidence grains, in which grain boundaries were unclear or segments of another grain were possibly visible, were not circled. The grain outlines were then converted to filled black shapes, rasterized, and exported for gray-scale image analysis in MATLAB at 300 pixels per inch resolution.

Biotite and hornblende inter-grow in all samples and could not be confidently separated for strain analyses. Instead, we considered all ferromagnesian phases together. If opaque minerals were surrounded by hornblende and/or biotite, they were not removed. If they were isolated, they were removed. These were digitized in Adobe Photoshop using colour-selective layer masks and complete thresholding to black. This way all composite grains were treated equivalently in image analysis. We considered all sizes first and then assessed just grains larger than  $0.5 \text{ mm}^2$  in area.

### ***Image Analysis***

To quantify shape changes, we used the the Gray Scale Image Analysis script (Bjørk, 2006), which piggybacks on MATLAB's native ImageProcessing toolbox. The MATLAB toolbox fits ellipses to the particles identified by the Gray Scale Image Analysis script. The output of the script is area, long and short axis lengths, long axis orientation, eccentricity, perimeter, and a number of other parameters for each ellipse (see Bjørk, 2006, for details). Orientation is given as the acute angle between the x-axis of the photo ( $0^\circ$  at the right side of the photo) and the long axis of the fitted ellipse. It ranges from  $-90^\circ$  (clockwise) to  $90^\circ$  (counterclockwise). Area is calculated directly from the number of pixels in the particle. We then converted the output from pixels to millimeters.

### ***$R_f/\phi$ Method for Visualizing Shape/Alignment Distributions***

The  $R_f/\phi$  method compares orientation and shape of particles (Ramsay and Huber, 1983). Shape is measured as aspect ratio ( $R_f$ ) and is plotted on the x-axis. Aspect ratio was calculated from long and short axis length results from image analyses. Orientation ( $\phi$ ) is the angle from a reference line, plotted on the y-axis. The comparison between aspect ratio and orientation allows for distinction between longer, more similarly aligned grains versus stubbier, randomly distributed grains, or any distribution in between. Figure 4.7 shows idealized, schematic, end-member distributions of shape and alignment. In dark green, the reference distribution has a wide range of grain long axis orientations and some intermediate peak aspect ratio (x-axis). Pure flattening could change this

distribution in two end-member ways. Rigid body rotation (i.e. strictly reorientation of grains) would retain the aspect ratio distribution while narrowing the range of orientations (medium green). If both intra-grain deformation and rotation occur (i.e. grains change shape and orientation), then long axes rotate into parallelism and aspect ratios increase (light green).

#### *Long Axes*

Depending on the behaviour and rheology of their matrix, phenocrysts may rotate into parallelism and shorten or lengthen depending on their initial orientation. An increase in the proportion of longest long axes indicates elongation in at least one direction, which corresponds to flattening if the flattening axis is also contained in the thin section plane.

#### *Aspect Ratio*

If plagioclase phenocrysts have experienced internal strain as well as primary igneous sorting, then simply using axis lengths may not distinguish effects of these processes. In this case, aspect ratio is a more useful measure of shape when combined with orientation and weaker phase changes. Depending on the original orientation of a grain in bulk flattening, its aspect ratio may increase or decrease, and may also be coupled with orientation change if rotation happens at the same time (Fig. 4.7).

#### *Grain Size*

Change in grain size is not a direct measure of strain. A general reduction in grain size is often observed in shear zones due to fracturing or recrystallization into new, smaller, higher-energy shapes (e.g. White et al., 1980). Decrease in area of phenocrysts is a complicated signal as it could also involve primary magmatic grain size trends. Abrupt changes in slope of median or average grain size versus distance along the transect may be a more useful measure of deformation-related grain size reduction. It is also possible that plagioclase grain size distributions change little with increasing strain if cataclasis and/or recrystallization are limited in plagioclase or if weaker phases take up intra-grain deformation and grain size reduction while plagioclase phenocrysts undergo rigid-body rotation.

### Orientation

The orientation of phenocryst long axes may be related to primary magmatic alignment or the result of deformation, which informed our field observations (interpretations and reasoning are discussed in more detail in Section 4.6.1). In the field, we noted that, closer to the NW edge of the pluton, orientation of mineral long axes as well as platy biotite become more aligned into parallelism with the pluton's edge.

The variability of each of these parameters and their components is also important for describing strain. For example, if the variability of long axis orientations decreases along the strain gradient but the aspect ratios and area remain constant, then the phenocrysts rotate into parallelism as rigid bodies. However, if instead the aspect ratios increase while long axis orientation variability decreases and area remains constant, we can infer non-rigid behaviour in plagioclase under bulk rock flattening. The long axes of the grains rotate toward a common orientation in both cases, but in the second case, the phenocrysts change their shape by internal deformation.

For  $R_f/\phi$  analyses, we chose the reference line as parallel to foliation or main mineral long axis alignment estimated visually. This was usually parallel to the base of the thin sections used in image analyses. Orientation measurements came directly from the image analysis output.

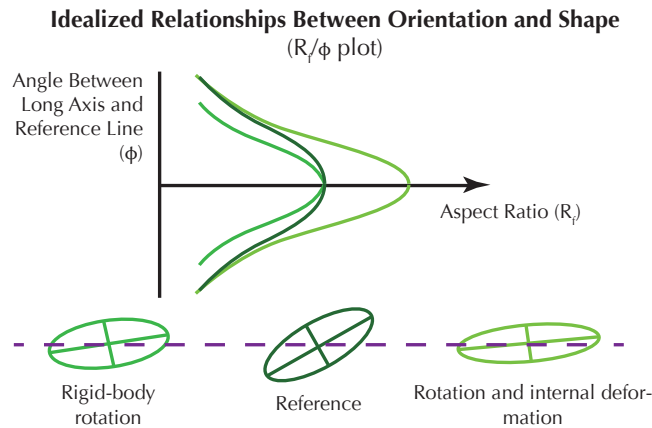


**Figure 4.7** The  $R_f/\phi$  method of Ramsay and Huber (1983) allows for comparison between different shape/alignment distributions. The y axis is orientation, given as angle from reference line. We chose the reference lines visually as foliation or main mineral alignment, if present. Shape is measured as aspect ratio, plotted on the x-axis. Three end-member distributions are illustrated here: darkest green shows a reference distribution from an undeformed sample with no preferred alignment of minerals. The medium green distribution shows the result of solely rigid body rotation, as might happen to rheologically strong phases in a bulk flattening regime. The lightest green distribution would result from simultaneous elongation and rotation of the grains measured. This would be the case in magmatic flow.

#### 4.4.2 Quantifiable Changes

Results of sample-scale studies in both the dominant plagioclase and the minor or rheologically weak but important mafic phases support field-scale observations and interpretations of a strain gradient from the interior to the edge of the pluton: plagioclase phenocrysts become smaller and more rare, and their preferred alignment becomes stronger (Fig. 4.8). Total mafic phases' mode remains constant at approximately a 10% coverage of thin section scan area, and grains larger than 0.5 mm<sup>2</sup> become more aligned toward the pluton's edge (Fig. 4.9). Table 4.1 details the  $p$  values of correlation of each variable with distance from the edge of the pluton. Northern unit values include all samples. Marginal northern unit values exclude MX23, which came from the interior of the northern unit (Fig. 4.1).

Correlation with Distance from Pluton Edge	Northern Unit	Marginal Northern Unit
Thin Section Area Occupied by Plagioclase Phenocrysts	$r = 0.68$ $p = 0.029$	$r = 0.80$ $p = 0.0091$
Plagioclase Alignment	$r = 0.88$ $p = 0.00081$	$r = 0.81$ $p = 0.0085$
Thin Section Area Occupied by Mafic Phases (all sizes)	$r = 0.22$ $p = 0.053$	$r = 0.50$ $p = 0.031$
Thin Section Area Occupied by Mafic Phases ( $\geq 0.5$ mm <sup>2</sup> )	$r = 0.65$ $p = 0.043$	$r = 0.72$ $p = 0.18$
Mafic Phases Alignment	$r = 0.79$ $p = 0.0061$	$r = 0.72$ $p = 0.031$
Mafic Phase Maximum Aspect Ratio	$r = -0.21$ $p = 0.56$	$r = 0.067$ $p = 0.84$

**Table 4.1** Correlations (Spearman's  $r$  and  $p$  values) for change in a variety of variables with distance from the NW edge of the San José Pluton. Values for the northern unit include results from MX23, near the south-central margin of the northern unit, while values for the marginal northern unit include only the 750 m closest to the pluton's edge (Fig. 4.1).

Results from the  $R_f/\phi$  method (Ramsay and Huber, 1983) allow us to distinguish different responses of plagioclase phenocrysts to bulk flattening (Fig. 4.10). The first distribution in Figure 4.10 is from MX23, the reference sample for the interior of the northern unit (Figs. 4.1 and 4.5). The middle 50% of orientation values fall between  $-25^\circ$  and  $25^\circ$ . Because this sample comes from about 2170 m away from the edge of the pluton, we interpret the orientation distribution as quantitative confirmation of field-based assessment of this sample as having minor preferential alignment of

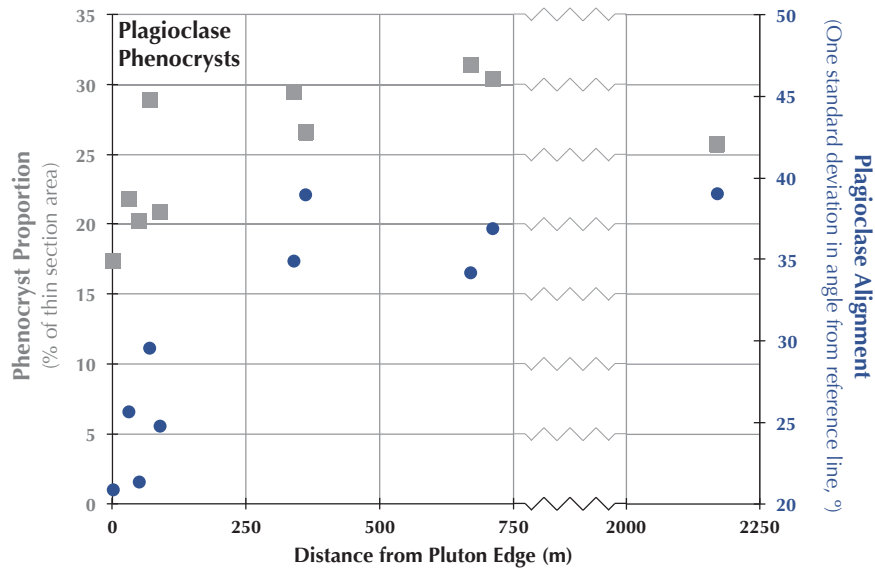


**Figure 4.8** Plagioclase abundance and grain size decrease along the strain gradient as shown by their decreasing proportion of thin section area (grey squares). The alignment noted in the field is significant also in thin section in terms of the decrease of the standard deviation of angle of plagioclase phenocryst long axes away from the visually estimated preferred alignment (blue circles).

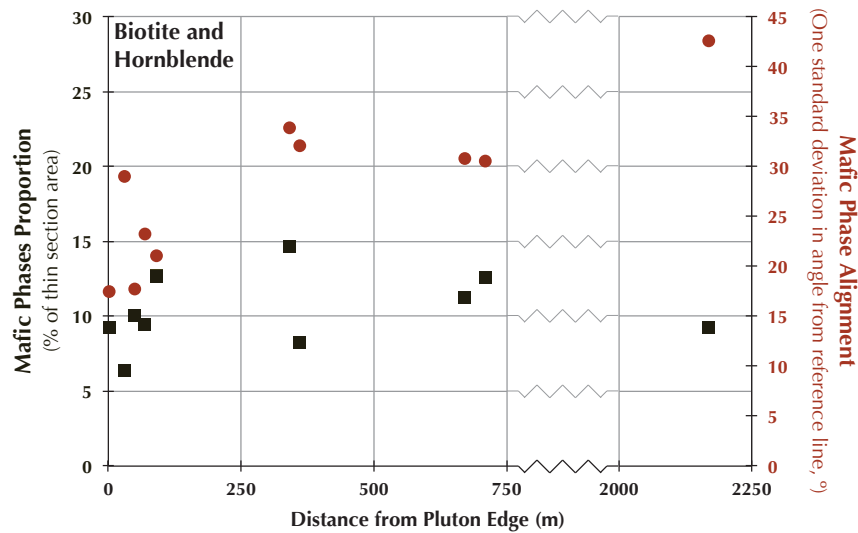


**Figure 4.9** Though abundance increases in terms of numbers of grains, total mode percent of mafic phases does not change significantly (within 95% confidence, dark brown squares). Mafic phase alignment noted in the field significantly increases toward the pluton's edge (as measured by the decrease in standard deviation of angle between grain long axes and foliation reference line, dark orange circles).

minerals and thus being undeformed. The distribution in MX08 (Fig. 4.10), taken 340 m from the NW edge of the pluton near the first appearance of aligned, elongated biotite (Section 4.3.2) shows a narrower range of common orientations (the middle 50% of values span  $40^\circ$ ) and higher maximum aspect ratios. This fits with the distribution expected for simultaneous elongation and rotation of phenocrysts drawn in light green in Figure 4.7. At the northwesternmost edge of the pluton, MX13 has an even narrower distribution of orientations (middle 50% between  $-13^\circ$  and  $13^\circ$  of foliation plane) and a lower maximum aspect ratio than the other two distributions (Fig. 4.10c). We interpret MX13 plagioclase phenocrysts to have undergone a combination of rigid body rotation (narrower orientation range, medium green end-member in Fig. 4.7) as well as internal deformation. In thin section, plagioclase grains in MX13 sometimes show patchy extinction as well as subgrain and new grain formation at grain boundaries. We suggest that the combination of microstructural and quantitative observations cannot have developed during initial emplacement as investigated phenocrysts were suspended in a magma but rather represent solid-state deformation resulting from the intrusion of the central and southern units of the San José pluton once the northern unit was solid (as interpreted by Murray, 1978; Johnson et al., 1999).

## 4.5 Grain-Scale Studies

Field observations and sample-scale analyses allow for bulk rock deformation to be contextualized and quantified. At the grain scale, strain and composition can be linked.

### 4.5.1 Grain Selection

We selected individual crystals for chemical analyses based on visibility of growth zoning and evidence of intra-grain deformation (Figs. 4.12 and 4.11). Plagioclase phenocrysts display a variety of growth zoning styles, including normal concentric zoning, oscillatory concentric zoning, chessboard zoning, and patchy zoning. Some grains have zoning cut by irregular resorption surfaces, and inclusion-rich horizons are common. Although grains often have similar zoning patterns to one another, no two grains show identical patterns. We therefore selected only grains with undeformed regions and curved regions which preserve an internal strain gradient. The complete gradient within one grain sets a background control on some of the influences on diffusion, such as crystallographic

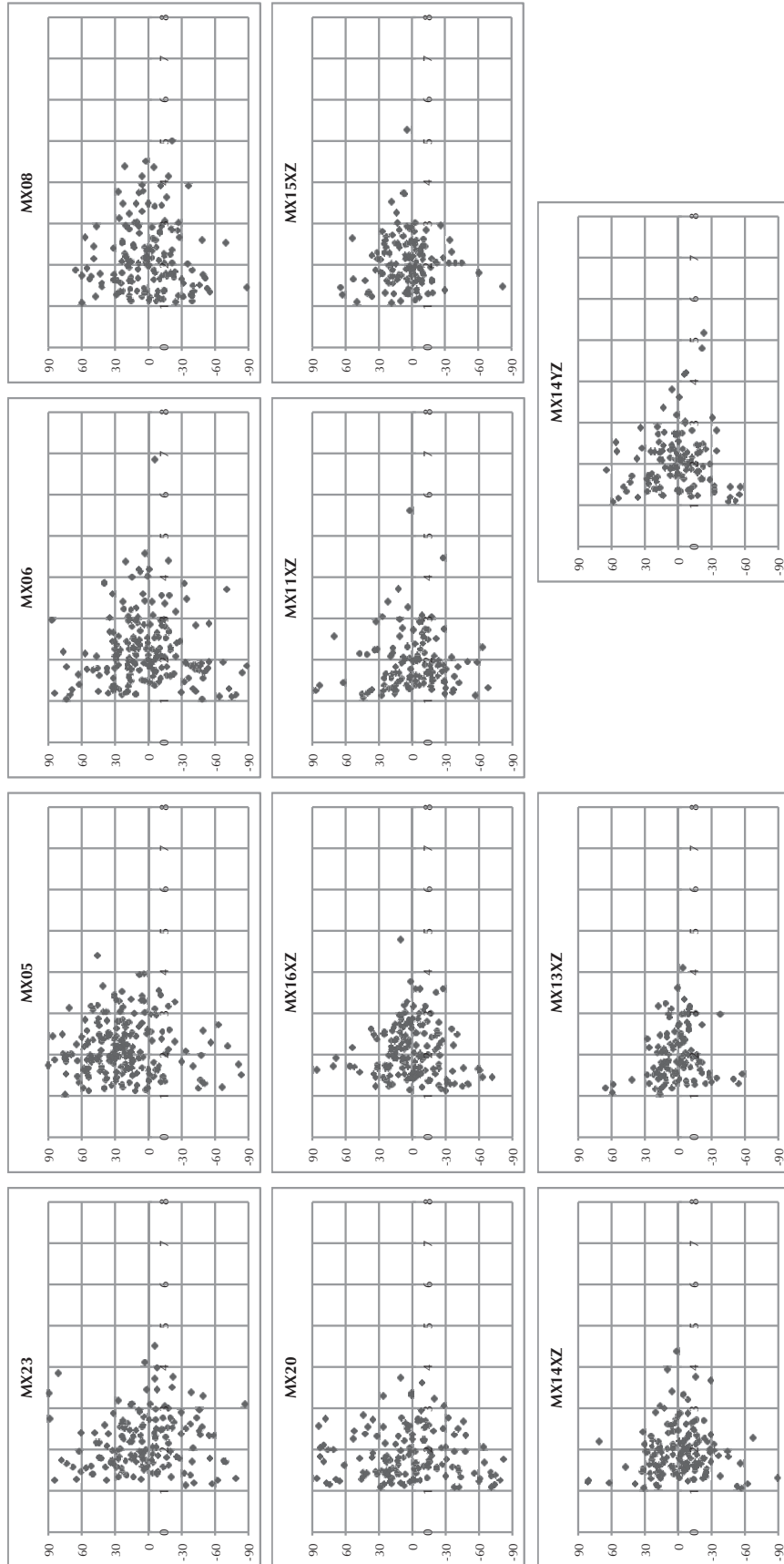


**Figure 4.10**  $R_f/\phi$  plots (Ramsay and Huber, 1983) from image analysis results of orientations and aspect ratios of plagioclase phenocrysts. See text for complete discussion. (MX14YZ is included among the otherwise XZ samples because grain BTW came from this sample, as discussed in Section 4.5.) All distributions are centered or nearly centered on the x-axis, indicating that thin section orientations were well-cut to capture the preferred phenocryst alignment.

orientation, zone boundary orientation, absolute composition, and twinning. Grains with no visible zoning or no evidence for internal crystal-plastic deformation were not considered since making a connection between deformation and element mobility would not be possible without both a measure of chemical and physical change. After preliminary analyses on the electron microprobe to determine if composition contrasts across zone boundaries were measurable, two grains were selected for full chemical analyses. One grain which underwent full analysis came from MX16, sampled 90 m from the NW edge of the pluton in an area where field-scale observations indicated that plagioclase played a small role in bulk flattening (Fig. 4.2e). This grain, called “MTL”, has curved growth twins and a region of subgrains that form a micro-shear zone that fully cuts through the crystal (Fig. 4.11a).

The second grain came from sample MX14, which was taken 30 m from the NW edge of the pluton and has biotite-defined foliation with some large phenocrysts (Fig. 4.2g). This grain, called “BTW”, has a gentle bend visible both in the shape of the phenocryst and as curved growth twins (Fig. 4.11b).

Both grains come from samples in which plagioclase shows signs of internal deformation but mostly accommodates bulk-flattening by rotation (Fig. 4.10).

#### **4.5.2 Strain Measurements in Individual Phenocrysts**

The heterogeneous deformation of MTL was interpreted from differing microstructural signatures. Each required individual approaches to estimate elongation parallel to the original long axis of the grain (Fig. 4.12). A region of bent twins was treated as linear strain: the ratio of deformed length to initial length of the growth twins. The region of subgrains is narrower than the rest of the grain, apparently shortened perpendicular to the long axis of the crystal (Fig. 4.11), so a length change could be estimated based assuming area preservation (plane strain). Then all elongations were added to find the total elongation of the grain at the zone boundary, giving a total integrated elongation of  $3.7 \pm 5\%$  at the composition zone boundary, as shown in Figure 4.12. The strain is localized in the hinge of the bend where three different regions accommodate extension with different deformation mechanisms. This area has a total elongation of  $11 \pm 2\%$ . The shortening direction is approximately NW-SE (vertical to this grain in the view of the thin section), which is consistent with the elongation direction measured in this XZ-oriented thin section parallel to the preferred long-axis orientations

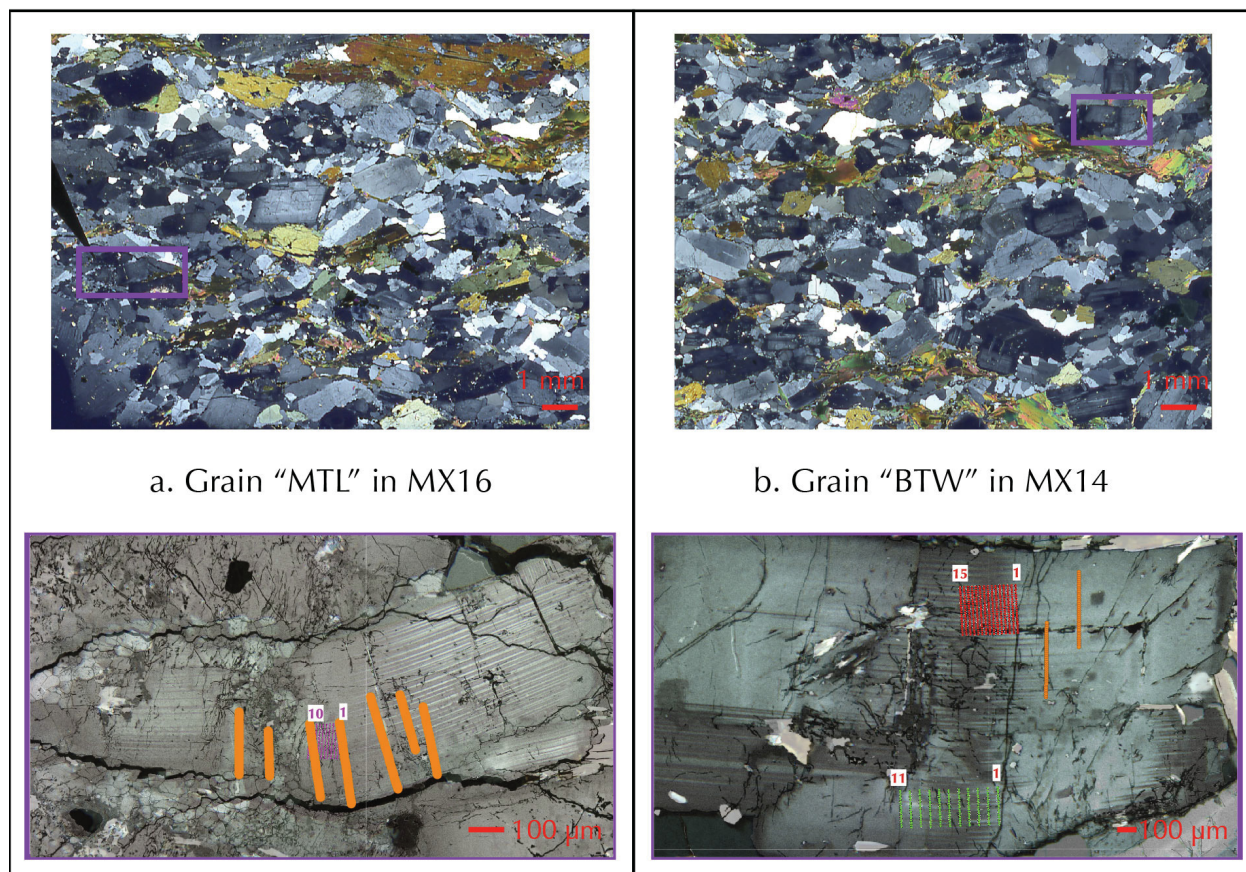


**Figure 4.11** The grains selected for chemical analysis have both internally deformed and undeformed regions which control for several factors that influence diffusion within a fully preserved micro-strain gradient. Top: Cross-polarized light thin section scans showing weak foliation, some preferred alignment, and context of grains analyzed. Bottom: Backscatter electron images overlain on cross-polarized light photomicrographs of MTL (**a.**, left) and BTW (**b.**, right) with microprobe analysis points in orange, and laser analysis points in magenta (MTL) and red and green (BTW). Line numbers mark the first and last lines of each laser point grid. Analysis location points are not mapped to scale. They are for general illustration purposes only.

observed in the field and perpendicular to the ENE-trending, southward-dipping foliation.

BTW displayed only bent twins. The change in angle of twins with respect to their initial orientation gave the angular shear which amounted to  $4 \pm 1^\circ$ .

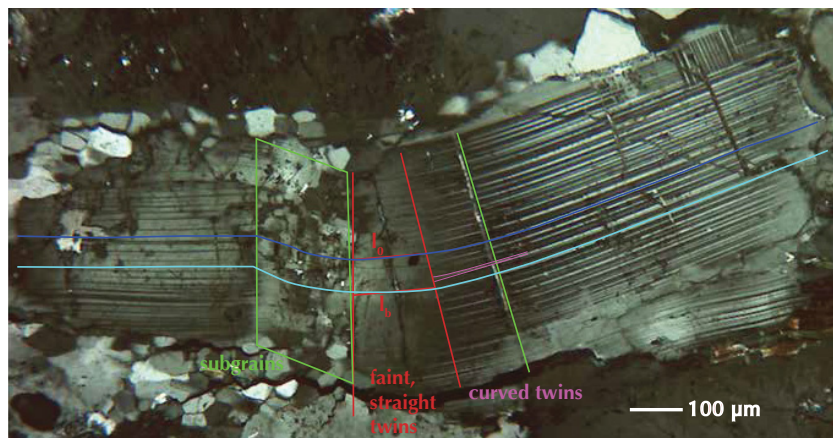


**Figure 4.12** Different deformation styles required different methods for measuring strain. Grain MTL from MX16 (90 m from pluton edge) exhibits all three styles found in the samples which underwent full chemical analysis. Curved twins were measured either as a change in angle or as a line length change through the bent region (magenta). More bent areas of grains were treated as simple extensional regions and again line lengths were compared (red). In areas of extensive subgrain formation where the grain appeared to be shortened in one direction, area comparison to an undeformed region of the grain was made to estimate line length change assuming plane strain (green). Dark blue line marks the reference line for linear strain. Cyan line marks the zone boundary where new length was measured.

### 4.5.3 Major Element Profiles

Electron microprobe analyses showed that the plagioclases analyzed are mostly  $An_{15}$  to  $An_{50}$ , mostly with very little K. For example, K content in BTW (MX14) ranges from 0.4% to 27% cation proportion ( $(K/(Na+Ca+K))$ ), with a median of 0.8%. The highest concentrations of potassium were found along fractures where potassic alteration replaces the magmatic plagioclase. Fe, Mg, and Ti were below their respective detection limits. Electron microprobe measurement locations are mapped in orange in Figure 4.11 and the results for Ca are plotted for MTL in Figure 4.13 along with the wavelength dispersive spectrometry (WDS) element map for Ca. For BTW, quantitative element maps provided higher resolution data than lines of point analyses. Profiles were plotted from grey-scale values from WDS element maps using ImageJ. The Ca map and profiles are given in Figure 4.14.

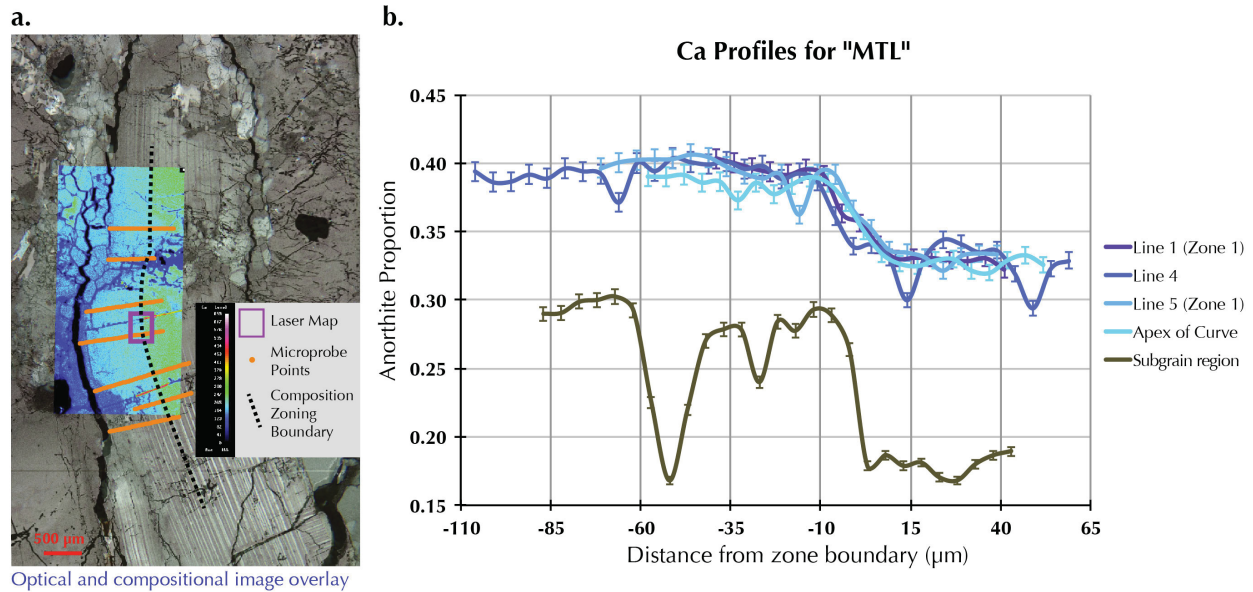


**Figure 4.13** **a.** Overlay of photomicrograph, electron backscatter image, Ca-concentration x-ray map, and locations of analyses. **b.** Measured concentrations for Ca along boundary-crossing transects of increasing deformation in “MTL” (MX16). Error bars represent analytical uncertainties, and colours indicate lines measured in areas of increasing strain (royal blue = undeformed, lower on image in (a); cyan = most deformed and higher in image in (a)).

#### 4.5.4 Minor and Trace Element Profiles

Minor and trace element concentrations in both grains are low. Average concentrations in BTW were Sr  $980 \pm 160$  ppm, Ba  $175 \pm 47$  ppm, and Pb  $7 \pm 3$  ppm (data for red raster in Figure 4.11). Sr gave the best results in both grains. Figure 4.15 shows the Sr concentrations measured at the points mapped in magenta in Figure 4.11. Figure 4.16a shows the Sr concentrations measured at the points mapped in red in Figure 4.11 and 4.16b shows the Sr concentrations measured at the points mapped in green.

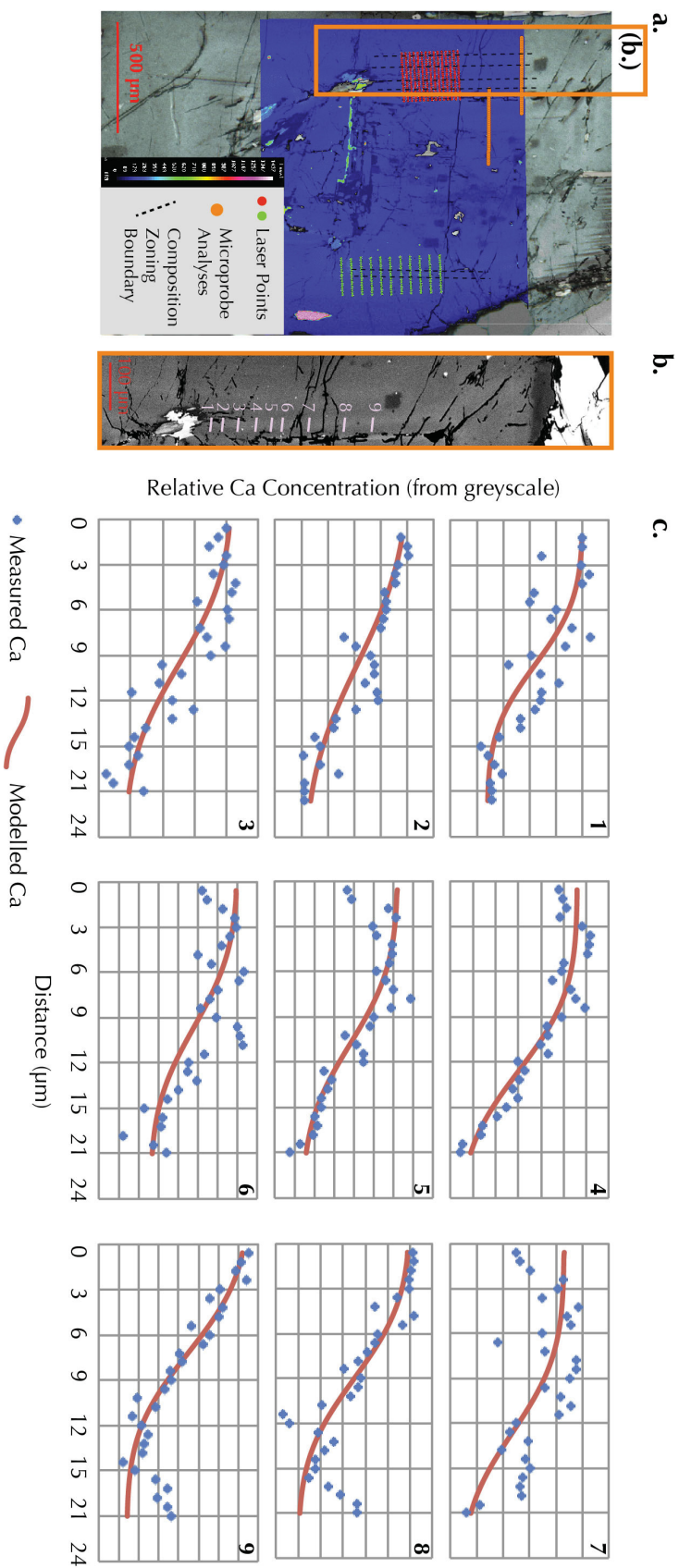


**Figure 4.14** Locations and measured concentrations for Ca along boundary-crossing transects of increasing deformation in “BTW” (MX14). **a.** Overlain photomicrograph with backscatter electron image basemap and Ca x-ray concentration map and analysis locations. **b.** Inset detailing greyscale image profiles keyed to numbers in (c). **c.** Concentration profiles as measured on greyscale concentration map with measured values in blue and models in red. Relative analytical uncertainty is approximated at 2%.

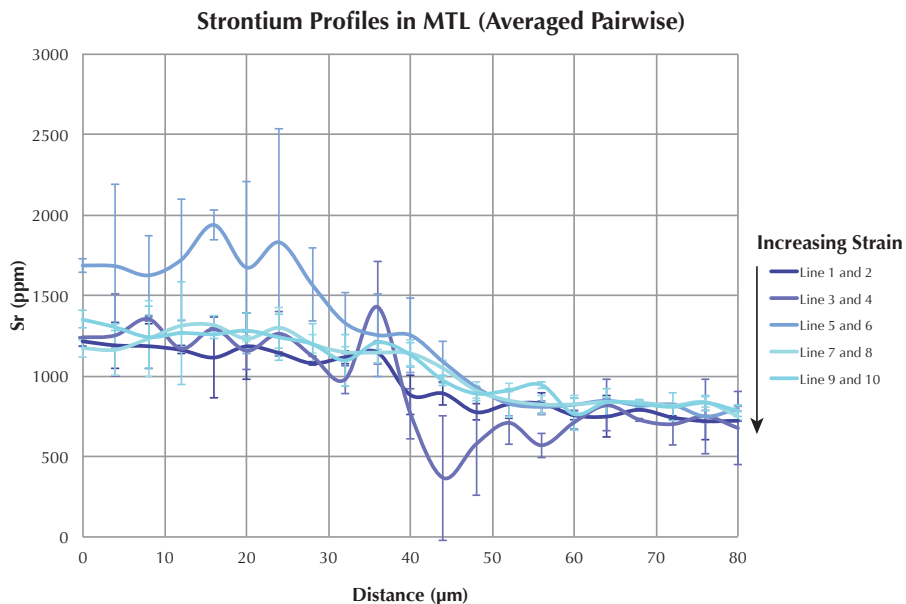


**Figure 4.15** Sr concentrations measured with LA-ICP-MS in increasingly strained portions of “MTL”, as located in magenta box in Figure 4.13a. Line colours qualitatively indicate strain in crystal at measurement locations with dark lines in undeformed regions and cyan lines in the most deformed regions. Error bars are uncertainty as given by 1 standard deviation about average values.

## 4.6 Evaluating Whether We Measured Deformation-Enhanced Element Mobility

### 4.6.1 Field Scale Conditions

#### *Assessing Strain: Solid State Deformation*

Vernon (2000) proposed a list of criteria to distinguish solid state and magmatic deformation in granitic rocks. He provides the following evidence for magmatic flow:

1. Parallel alignment of elongate, euhedral crystals with no internal deformation
2. Tilting of these crystals
3. Minor strain of inter-grain material between tilted or aligned crystals
4. Plastic-deformation-free elongation of microgranitoid enclaves
5. Signs of magmatic flow such as foliations and elongated microgranitoid enclaves around xenoliths

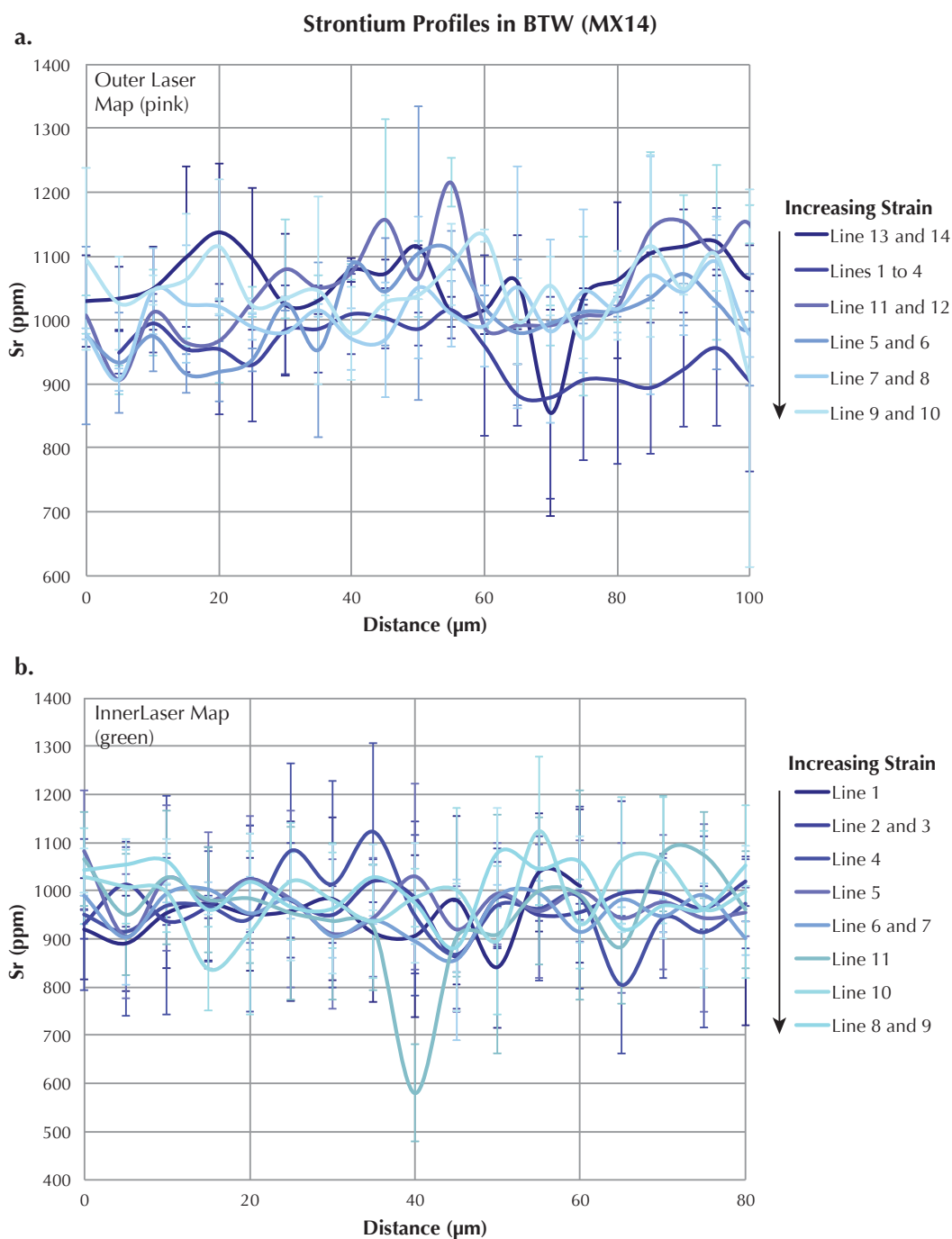


**Figure 4.16** Sr profiles measured in both laser point sets illustrated in Figure 4.14. Line colours qualitatively indicate strain in crystal at measurement locations with dark lines in undeformed regions and cyan lines in the most deformed regions. **a.** Results from outer map plotted in pink in 4.14. Error bars are uncertainty as given by 1 standard deviation about average values. **b.** Results from inner map plotted in green in Figure 4.14. Error bars are uncertainty as given by 1 standard deviation about averaged values from multiple lines of points. For measurements in lines which were not averaged with any other lines, the error bars represent 2 standard errors as estimated by LA-ICP-MS data processing software Iolite based on count statistical error. Since this is always an underestimate of uncertainty, we use two standard errors.

6. Schlieren

He goes on to list signs of solid-state deformation (Vernon, 2000):

1. Intra-grain deformation and recrystallization
2. Recrystallized regions adjacent to larger grains (“tails” on porphyroclasts)
3. Recrystallized aggregates are elongated
4. Reduction in grain size
5. Less deformed relict grain surrounded by anastomosing fine-grained folia
6. Microcline twinning
7. Myrmekite, particularly at the edges of K-feldspar
8. Flame perthite
9. Boudinaged stronger minerals, particularly with recrystallized aggregates of weaker phases between boudins
10. Anastomosing foliation that passes through enclaves rather than going around them
11. Locally mylonitized zones in a highly heterogeneous strain field at various scales
12. Evidence of both brittle and ductile deformation such as fragmented grains with filled fractures or feldspar grains in quartz ribbons
13. Reset geochronological age in biotite (i.e. younger than intrusion age)

Our observations of a transition from linear alignment of magmatic minerals to planar alignment of the same minerals but with ample biotite (Section 4.3.2) closely match these criteria. In samples taken farther from the NW pluton-wall rock contact, we conclude that aligned, euhedral hornblende and plagioclase phenocrysts that show no signs of internal deformation are instead indicative of

magmatic flow. Quartz shows minor sweeping extinction in some samples, which can be considered minor strain of interstitial minerals between aligned, elongate phenocrysts.

We also observe many of the criteria Vernon (2000) gives for solid state deformation. Some criteria are not applicable to these samples since no K-feldspar was found. Among the applicable criteria, all were observed. We see internal deformation of quartz, plagioclase, and biotite, particularly bending of plagioclase and biotite and recrystallization of quartz (criterion 1). Deformed grains sometimes have recrystallized tails (criterion 2). Recrystallized aggregates, particularly quartz, are elongated (criterion 3). We observe grain size decrease as a decrease in the proportion of large phenocrysts (criterion 4, Section 4.4.2). Biotite folia increasingly anastomose around plagioclase grains and multi-mineralic lozenge-shaped regions (criterion 5, Fig. 4.2). Criterion 8 outlines boudinage of strong minerals and highlights formation of recrystallized aggregates of weaker minerals within the boudins. We observed quartz- and minor biotite-filled regions between portions of plagioclase grains that appear to have been pulled apart, which could equally be interpreted as satisfying criterion 8 or criterion 12. In this case, Vernon (2000) lists fractured and fragmented plagioclase with quartz-filled fractures. In either case, these grains allow us to conclude that deformation was primarily solid state, in agreement with previous work (e.g Johnson et al., 2003, 2004; Vernon et al., 2004). Our field and microstructural observations are consistent with Johnson et al. (2004) in confirming that deformation in the carapace of the San José pluton is unequivocally solid state superimposed on primary magmatic textures. Vernon (2000) also concludes in one of several case studies that the San José Pluton is an example of “solid state flow superimposed on magmatic flow”.

The grains analyzed for chemistry and grain-scale strain came from samples with connected biotite, well-aligned, rounded plagioclase phenocrysts. The grains also display internal deformation consistent with bulk rock flattening, so we confidently attribute their strain to solid-state deformation.

### ***Evidence of Fluid Overprint***

In order to confidently evaluate the influence of deformation on element mobility, we must first exclude alternative element mobility enhancements, particularly fluid overprint. The increasing abundance of biotite with increasing strain at the expense of hornblende within a statistically consistent mafic mode percent indicates the addition of water and K during deformation. If such a fluid pervaded, we would expect widespread alteration of plagioclase to muscovite. We observe

very limited alteration in very few large plagioclase phenocrysts in which the centers of the grains are altered. The grains analyzed were clear of any evidence of such alteration. A more widespread alteration feature observed is K-enrichment along fractures in plagioclase. These fracture-related, altered regions crosscut growth zoning and have diffuse boundaries into the plagioclase grains. Although we cannot determine the exact timing of this alteration, their K-content suggests they were synchronous with the same fluids that allowed biotite to replace hornblende. We therefore conclude that fluids were present and did cause alteration, but the effect on the otherwise nearly K-free plagioclase compositions is distinctly identifiable by its K-signature. This allows us to differentiate between compositional effects caused by deformation and those resulting from fluid overprinting initial compositions.

In theory, plagioclase compositions could all be fluid-altered. If this were the case, we would expect to see a change in alteration with distance from the pluton's edge, the fluid source. We tested this by calculating the P-T conditions of formation from major element partitioning between amphibole and plagioclase: if high temperature and high pressure<sup>1</sup> of pluton emplacement are preserved and there is no trend in these measures with distance from the edge of the pluton, we can trust apparent changes in composition with deformation to be strain-related.

Results using the Holland and Blundy (1994) plagioclase-amphibole thermobarometer are given in Table 4.2 and plotted on Figure 4.17. Neither temperatures nor pressures are different with 95% confidence among all the samples measured, and all values are uniformly high. This indicates that fluids did not reset the thermobarometer after it recorded emplacement conditions. Fluids were present at the time of deformation in order for biotite to grow but not completely replace hornblende. There was also not systematic albitization nor potassic alteration toward the edge of the pluton, as evidenced by similar anorthite proportions (Table 4.2). The preservation of magmatic minerals and the robust values of  $700 \pm 28^\circ\text{C}$  and  $192 \pm 32 \text{ MPa}$  suggest that these were the conditions during deformation and any chemical changes measured can be confidently attributed to deformation rather than fluid overprint. We refine the similar but less well constrained estimates given by Vernon et al. (2004) of about  $680^\circ\text{C}$  and  $270 \text{ MPa}$  for deformation conditions. Finally, thermobarometry data indicate that any deformation post-dating emplacement-related deformation described here occurred at or below greenschist facies and did not overprint the structures or chemistry we explored.

---

<sup>1</sup>high relative to values which would come from alteration

Sample	Distance from pluton edge (m)	An proportion	Temperature (°C)	Pressure (MPa)
MX23	2170	0.27	703 ± 40	250 ± 40
MX05	710	0.30	709 ± 33	206 ± 28
MX08	340	0.31	692 ± 36	189 ± 30
MX16	90	0.29	689 ± 10	193 ± 32
MX11	70	0.27	683 ± 28	198 ± 26
MX14	30	0.31	711 ± 28	189 ± 28
MX13	1	0.29	703 ± 32	179 ± 9
Average		0.29	700 ± 28	192 ± 32

**Table 4.2** Average compositions, temperatures, and pressures in order of increasing strain and decreasing distance from NW pluton edge. Temperatures and pressures were calculated using the plagioclase-amphibole thermobarometer of Holland and Blundy (1994) for the reaction edenite + albite = richterite + anorthite. Uncertainties are one standard deviation about the average temperature and pressure determined for each sample's multiple analyses.

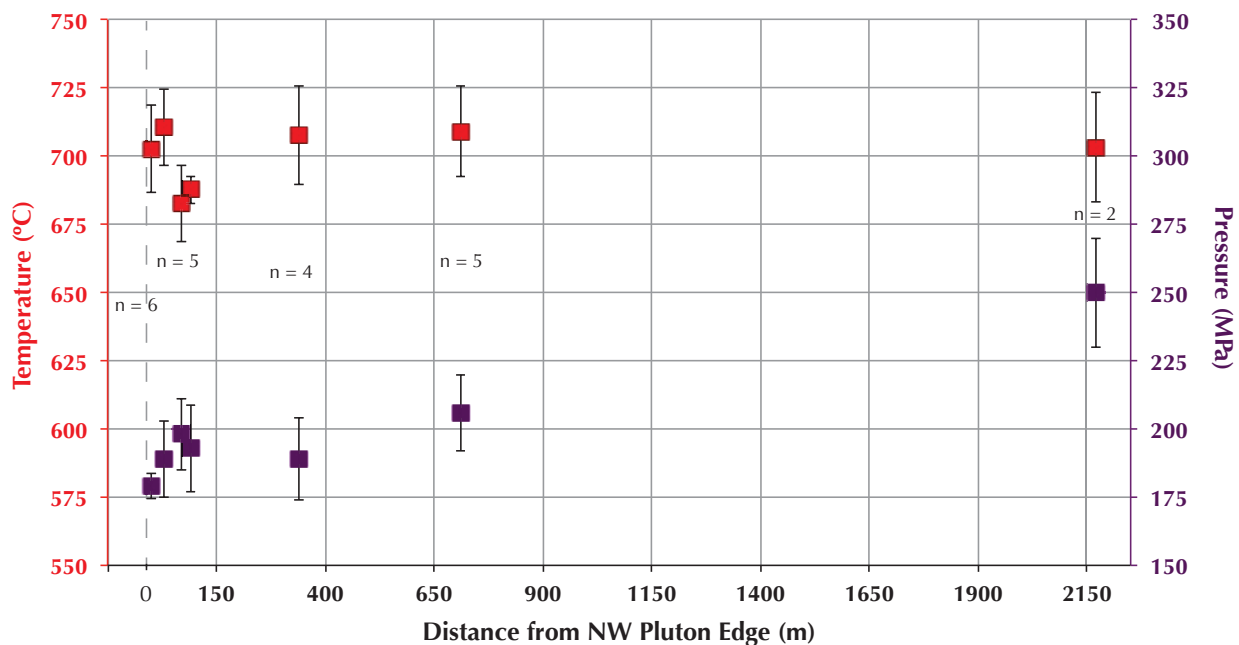


**Figure 4.17** Temperature (bright red) and pressure (dark purple) results from the interior of the northern unit to the NW edge of the pluton calculated using the thermobarometer of Holland and Blundy (1994). Number of analyses per sample are listed, with the three penultimate samples each having 5 analyses. Although it appears that pressure decreases, statistical analysis (ANOVA) reveals that this is not significant beyond uncertainty at 95% confidence.

### 4.6.2 Grain Scale Conditions

#### *Major Elements Not Affected*

In both grains, microprobe measurements show that primary compositional zoning is preserved in undeformed regions of the crystal as a sharp compositional contrast with some smoothing by diffusion between the growth zones. This re-equilibration took place immediately after crystal formation and continued until the grain passed through the closure temperature for diffusion (e.g. Costa et al., 2003). If deformation enhanced diffusion, smoothed profiles would be expected, and their slopes should flatten with increasing deformation (see Section 2.6.2). Instead, profiles measured in deformed regions of the crystals are indistinguishable from those measured in less and undeformed parts (Figs. 4.13 and 4.14).

The lack of measurable enhancement among the major elements may be caused by their relatively sluggish movement in plagioclase at 700°C. In order for any major elements to move, the other major elements must also move in order to maintain charge balance in the coupled substitution  $\text{Ca} + \text{Al} \rightleftharpoons \text{Na} + \text{Si}$ . Interdiffusion of CaAl - NaSi is simply too slow to be measurably affected. At 700°C, the diffusion rate in these samples was  $\sim 1.94 \cdot 10^{-31} \text{ m}^2/\text{s}$ , which is  $\sim 6.11 \cdot 10^{-12} \text{ } \mu\text{m}^2/\text{Myr}$ .

If deformation-enhanced element mobility could be measured in naturally deformed plagioclase phenocrysts, we would expect to see it in trace elements which should develop more pronounced differences with increasing strain due to their lower activation energies and higher diffusivities (see Fig. 2.7 in Chapter 2).

#### *Minor and Trace Elements Not Affected*

Minor and trace elements can move by vacancy migration, interstitial mechanisms, and through dislocation “pipes” (Love, 1964), which leads to higher diffusion coefficients and more efficient transport. Trace element transects (Figs. 4.15 and 4.16) show considerable scatter in measured concentrations. The scatter appears unsystematic, random, and does not correlate with fractures, inclusions, or strain measurements. We interpret this to mean that it is a result of analytical uncertainty. The amplitude of the scatter hinders any identification of trends but can be reduced by averaging comparable lines (similar location within the intra-grain strain gradient, crossing same features, etc.). Even then, although we expected elements such as Sr, Ba, Pb, Rb, and Eu to show

differential acceleration, we do not see the expected trends. (Rb and Eu are near or at detection limit even with LA-ICP-MS.) Instead of increasingly smooth profiles measured in increasingly strained regions of plagioclase phenocrysts (as expected from theoretical models presented in Chapter 2), all profiles within each grain (or grain region in the case of BTW) are identical within uncertainty. The scatter in trace element concentrations is large, apparently unsystematic, and cannot be accounted for by our analytical methods, grain effects such as inclusions or fractures, nor unequivocally attributed to strain. It appears that with the smallest beam size of the LA-ICP-MS, required to obtain the necessary spatial resolution, the analytical uncertainty (i.e. the data scatter) is too high, and we can not detect the subtle changes in compositional contrast between zones with increasing strain. Although a larger beam size would likely reduce the scatter, the diffusion profile is only  $\sim 50$   $\mu\text{m}$  in length. Several analysis spots are required along this profile to model it accurately, so a larger beam size would not solve this issue.

### 4.6.3 Pluton Cooling

Concentration profiles for Sr yielded the cleanest trace element results from which we modelled pluton cooling rate. It took  $1550 \pm 100$  years to cool from emplacement temperatures of  $700 \pm 28$   $^{\circ}\text{C}$  to the Sr closure temperature of  $550^{\circ}\text{C}$  for albite (Cherniak and Watson, 1992), at a regional cooling rate of about  $40^{\circ}\text{C}/\text{Myr}$  (Schmidt et al., 2009). This is nearly in agreement with our calcium results, which suggest  $1800 \pm 150$  years.

## 4.7 Conclusions and Implications

In this study, we tested out theoretical predictions. detailed in Chapter 2, that deformation enhances element mobility by investigating the relationship between strain and equilibration between compositional growth zones in plagioclase. We carried out detailed strain and chemical investigations on the variably deformed carapace of the San José pluton, in the Peninsular Ranges Batholith of northern Baja California.

The combination of large, growth-zoned plagioclase phenocrysts in a fully exposed, low-strain solid state deformation gradient including complete intra-grain strain gradients show that the selected field site is a perfect setting to test for strain-enhanced element mobility in plagioclase. Furthermore,

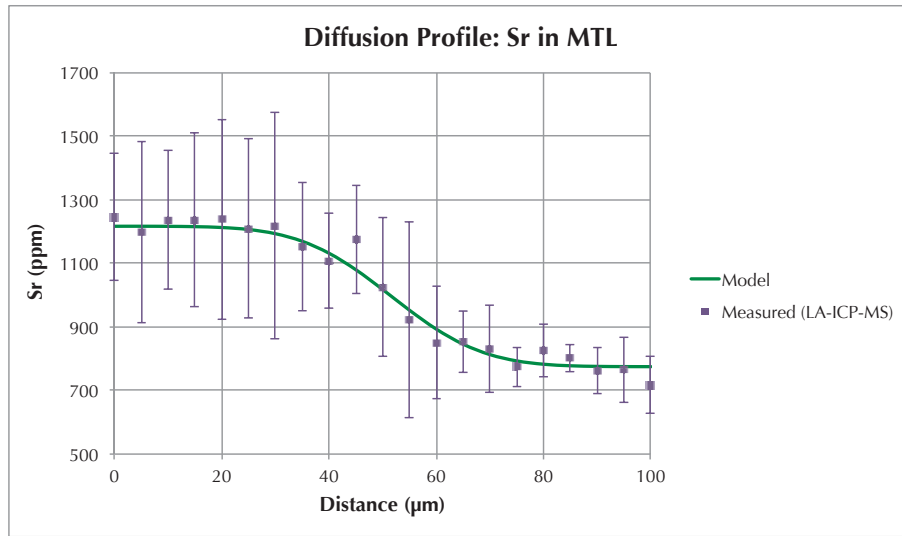


**Figure 4.18** Because a strain enhancement of diffusion was not measured at low strain, diffusion profiles in Sr and Ca from the undeformed parts of the crystals and less deformed parts of the laser maps could be used to model cooling. Profiles in MTL show clear results of about 1500 to 1900 years.

thermobarometry and mineral compositions indicate fluid overprint is not an issue in this setting. Microstructural analyses point to solid state deformation overprinting magmatic fabric as the main deformation even causing intra-grain strain. As such, bulk rock strain can be tied directly to single grain solid state deformation. Despite the perfect setting, major, minor, and trace element diffusion profiles across growth zone boundaries within each grain showed no significant change with strain, but did display the classic shape of diffusion of an initially stepped concentration contrast.

We conclude that in this study, the variables of initial concentration contrasts, element compositions, low strain, and rapid cooling (as fixed by the field site) do not allow for the effect of diffusion to be identified, nor quantified, and indicate that with present methods, low strain does not measurably enhance element mobility in plagioclase. Analytical restrictions are the primary cause for our inability to evaluate the effect of strain on element mobility, and future improvements may allow the effect to be confidently determined.

---

## Concluding Questions and Future Work

---

The field setting selected for this study based on initial criteria for zoned plagioclase phenocrysts in a plagioclase-dominated rock with a complete strain gradient, bulk rock and grain-scale deformation characteristics, thermal history, and grain size all appeared ideal for this study. We used the highest resolution analytical methods available to us. Deformation must enhance element mobility, as determined from first principles (Chapter 2), but it appears to be at or below the detection limit of our current technology in this setting of clean feldspars with small concentration contrasts which enjoyed only very small strain (Chapter 4). A variety of variables contribute to this, but this study remains outside the conditions in which strain-enhanced diffusion is measurable (Fig. 5.1). The shape of this condition-space in hyperspace of different variables remains to be determined, but some aspects of its edges are already known. For example, higher strain would likely obliterate zoning and future work should investigate other low-strain feldspars with higher trace element concentrations and larger compositional contrasts. Another possibility is to deform growth-zoned feldspars in the lab where duration, temperature, and strain can be stepped to best determine ideal conditions for strain-enhanced diffusion.

Strain will always have a subtle effect on diffusion rate: the strain energy contribution is limited by the elastic limit of interatomic bonds, and acts only as a subtraction from the activation energy for

diffusion (Eq. 2.2). A change in temperature ( $T$ ) can have a greater effect since it is a division factor rather than an addition or subtraction and is further magnified by  $R$ , the universal gas constant. This may be an additional explanation of the subtlety of a strain-signature in the natural samples investigated but also provides a useful basis for applying existing petrologic tools. Whereas major elements already have relatively low diffusion rates and high activation energies, the effect of strain on these quantities is not enough to disturb their diffusion. Thus, geobarometers, thermometers can still be used to determine the pressure and temperature conditions in question. Then, the trace elements, whose activation energies are proportionally more reduced than those of major elements even by permissibly small by strain, can be used to infer an approximate strain rate using the method developed in Section 2.6.2.

Changing the variable of the analytical tool used could also help constrain the shape of measurable deformation-enhanced element mobility in multivariate space. A very powerful instrument with low detection limit and high spatial resolution is secondary ion mass spectrometry (SIMS). This technique was not available, and brings its own set of analytical complications which would need to be individually evaluated. Still, it would be a promising avenue for future work.

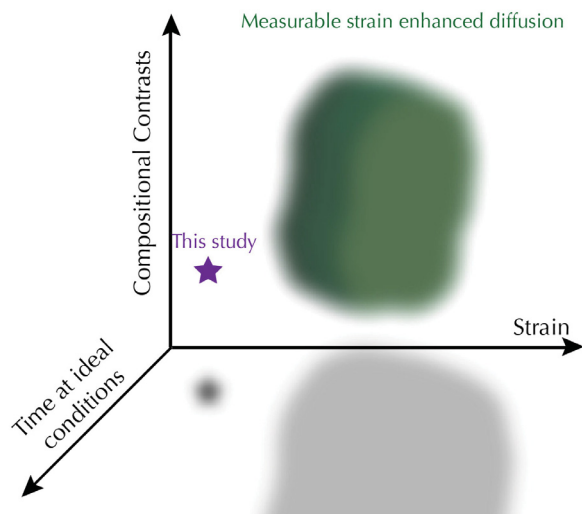


**Figure 5.1** Detection of deformation-enhanced element mobility depends on a variety of variables. Three variables that seem to have been most important in this study were time spent at optimal enhancement conditions, strain, and composition contrasts. Other influential variables are instrument sensitivity, pressure, temperature, primary concentrations, and the rates of change in each of these variables with time. Future studies must define the boundaries of the hyper-ameboid of conditions in which deformation measurably enhances element mobility such that diffusion-based tools can either be confidently applied or re-evaluated.

In summary, the geologist's toolkit of thermobarometers and geochronometers are not compromised in plagioclase in low strain rocks. However, the search for a method to measure duration of deformation to estimate strain rate in the rock record remains an open pursuit.

---

## Bibliography

---

- Alsleben, H., Wetmore, P., Schmidt, K., Paterson, S., Melis, E., 2008. Complex deformation during arc-continent collision: Quantifying finite strain in the accreted alisitos arc, Peninsular Ranges batholith, Baja California. *Journal of Structural Geology* 30 (2), 220–236.
- Balluffi, R. W., Ruoff, A. L., 1963. On strain-enhanced diffusion in metals I: Point defect models. *Journal of Applied Physics* 34 (6), 1634–1647.
- Bhattacharyya, P., Hudleston, P., 2001. Strain in ductile shear zones in the caledonides of northern sweden: A three-dimensional puzzle. *Journal of Structural Geology* 23 (10), 1549–1565.
- Bjørk, T. E., 2006. Gray Scale Image Analysis in 2006 Image Analysis Program for use with MATLAB.  
URL [http://folk.uio.no/torbjoeb/image\\_analysis](http://folk.uio.no/torbjoeb/image_analysis)
- Blackburn, T., Shimizu, N., Bowring, S. A., Schoene, B., Mahan, K. H., 2012. Zirconium in rutile speedometry: New constraints on lower crustal cooling rates and residence temperatures. *Earth and Planetary Science Letters* 317, 231–240.
- Blundy, J., Wood, B., 2003. Partitioning of trace elements between crystals and melts. *Earth and Planetary Science Letters* 210 (3), 383–397.
- Brady, J. B., 1983. Intergranular diffusion in metamorphic rocks. *Am J Sci A* 283, 181–200.
- Brady, J. B., Cherniak, D. J., 2010. Diffusion in minerals: An overview of published experimental diffusion data. *Reviews in Mineralogy and Geochemistry* 72 (1), 899–920.
- Brown, A. F., Blackburn, D. A., 1963. Apparent enhancement of diffusion coefficients in plastically deformed metals. *Acta Metallurgica* 11 (9), 1017–1021.
- Büttner, S. H., 2005. Deformation-controlled cation diffusion in compositionally zoned tourmaline. *Mineralogical Magazine* 69 (4), 471–490.
- Büttner, S. H., Kasemann, S. A., 2007. Deformation-controlled cation diffusion in tourmaline: A microanalytical study on trace elements and boron isotopes. *American Mineralogist* 92 (11), 1862–1874.

- Cherniak, D., Watson, E., 1992. A study of strontium diffusion in K-feldspar, Na-K feldspar and anorthite using Rutherford backscattering spectroscopy. *Earth and Planetary Science Letters* 113 (3), 411–425.
- Cherniak, D. J., 2010. Cation diffusion in feldspars. *Reviews in Mineralogy and Geochemistry* 72 (1), 691–733.
- Christensen, J. N., Selverstone, J., Rosenfeld, J. L., DePaolo, D. J., 1994. Correlation by Rb-Sr geochronology of garnet growth histories from different structural levels within the Tauern Window, Eastern Alps. *Contributions to Mineralogy and Petrology* 118 (1), 1–12.
- Cohen, M., 1970. Self-diffusion during plastic deformation. *Bulletin of the Japan Institute of Metals* 9 (5), 271–278.
- Costa, F., Chakraborty, S., Dohmen, R., 2003. Diffusion coupling between trace and major elements and a model for calculation of magma residence times using plagioclase. *Geochimica et Cosmochimica Acta* 67 (12), 2189–2200.
- Dodson, M. H., 1973. Closure temperature in cooling geochronological and petrological systems. *Contributions to Mineralogy and Petrology* 40 (3), 259–274.
- Dowty, E., 1980. Crystal-chemical factors affecting the mobility of ions in minerals. *American Mineralogist* 65, 174–182.
- Eiler, J. M., Baumgartner, L. P., Valley, J. W., 1992. Intercrystalline stable isotope diffusion: A fast grain boundary model. *Contributions to Mineralogy and Petrology* 112 (4), 543–557.
- Fara, H., Balluffi, R. W., 1958. Analysis of diffusion in media undergoing deformation. *Journal of Applied Physics* 29 (7), 1133–1134.
- Fick, A., 1855. Ueber diffusion. *Annalen der Physik* 170 (1), 59–86.
- Fortier, S. M., Giletti, B. J., 1989. An empirical model for predicting diffusion coefficients in silicate minerals. *Science* 245 (4925), 1481–1484.
- Fossen, H., 2010. *Structural geology*. Cambridge University Press.
- Gleason, G. C., Tullis, J., 1995. A flow law for dislocation creep of quartz aggregates determined with the molten salt cell. *Tectonophysics* 247 (1), 1–23.
- Grove, T. L., 1982. Use of exsolution lamellae in lunar clinopyroxenes as cooling rate speedometers: an experimental calibration. *American Mineralogist* 67 (3-4), 251–268.
- Hirth, G., Tullis, J., 1992. Dislocation creep regimes in quartz aggregates. *Journal of Structural Geology* 14 (2), 145–159.
- Hodges, K. V., 1991. Pressure-Temperature-Time Paths. *Annual Review of Earth and Planetary Sciences* 19, 207–236.
- Holland, T., Blundy, J., 1994. Non-ideal interactions in calcic amphiboles and their bearing on amphibole-plagioclase thermometry. *Contributions to Mineralogy and Petrology* 116 (4), 433–447.
- Johnson, S. E., Fletcher, J. M., Fanning, C. M., Vernon, R. H., Paterson, S. R., Tate, M. C., 2003. Structure, emplacement and lateral expansion of the San José tonalite pluton, Peninsular Ranges batholith, Baja California, México. *Journal of Structural Geology* 25 (11), 1933–1957.

- Johnson, S. E., Marsh, J. H., Vernon, R. H., 2008. From tonalite to mylonite: Coupled mechanical and chemical processes in foliation development and strain localization. *Journal of the Virtual Explorer* 30, 3–32.
- Johnson, S. E., Tate, M. C., Fanning, C. M., 1999. New geologic mapping and SHRIMP U-Pb zircon data in the Peninsular Ranges batholith, Baja California, Mexico: Evidence for a suture? *Geology* 27 (8), 743–746.
- Johnson, S. E., Vernon, R. H., Upton, P., 2004. Foliation development and progressive strain-rate partitioning in the crystallizing carapace of a tonalite pluton: Microstructural evidence and numerical modeling. *Journal of Structural Geology* 26 (10), 1845–1865.
- Kramar, N., Cosca, M. A., Hunziker, J. C., 2001. Heterogeneous  $^{40}\text{Ar}^*$  distributions in naturally deformed muscovite: In situ UV-laser ablation evidence for microstructurally controlled intragrain diffusion. *Earth and Planetary Science Letters* 192 (3), 377–388.
- Law, R. D., Schmid, S. M., Wheeler, J., 1990. Simple shear deformation and quartz crystallographic fabrics: A possible natural example from the Torridon area of NW Scotland. *Journal of Structural Geology* 12 (1), 29–45.
- Lee, C. H., Maddin, R., 1961. Effect of torsional deformation on self-diffusion in silver. *Journal of Applied Physics* 32 (10), 1846–1851.
- Lee, J. K. W., 1995. Multipath diffusion in geochronology. *Contributions to Mineralogy and Petrology* 120 (1), 60–82.
- Levien, L., Prewitt, C., Weidner, D., 1980. Structure and elastic properties of quartz at pressure. *American Mineralogist* 65, 920 – 930.
- Lisle, R. J., 1985. *Geological Strain Analysis: A Manual for the  $R_f/\phi$  Method*. Pergamon, Oxford.
- Love, G. R., 1964. Dislocation pipe diffusion. *Acta Metallurgica* 12 (6), 731–737.
- Mookerjee, M., Peek, S., 2014. Evaluating the effectiveness of Flinn’s k-value versus Lode’s ratio. *Journal of Structural Geology* 68, 33–43.
- Müller, W., Aerden, D., Halliday, A. N., 2000. Isotopic dating of strain fringe increments: Duration and rates of deformation in shear zones. *Science* 288 (5474), 2195–2198.
- Murray, J. D., 1978. The structure and petrology of the San José pluton, northern Baja California, México. Unpublished Ph.D. thesis, Pasadena, California Institute of Technology.
- Nicolas, A., Poirier, J.-P., 1976. *Crystalline plasticity and solid state flow in metamorphic rocks*. Wiley London.
- Pabst, W., Gregorová, E., 2013. Elastic properties of silica polymorphs—a review. *Ceramics-Silikaty* 57, 167.
- Platt, J. P., Behr, W. M., 2011. Lithospheric shear zones as constant stress experiments. *Geology* 39 (2), 127–130.
- Poirier, J.-P., 1985. *Creep of Crystals: High temperature deformation processes in metals, ceramics and minerals*. Cambridge Earth Science Series. Cambridge University Press.

- Porter, D. A., Easterling, K. E., 1989. Phase Transformations in Metals and Alloys. Van Nostrand Reinhold International.
- Prior, D. J., Boyle, A. P., Brenker, F., Cheadle, M. C., Day, A., Lopez, G., Peruzzo, L., Potts, G. J., Reddy, S., Spiess, R., 1999. The application of electron backscatter diffraction and orientation contrast imaging in the SEM to textural problems in rocks. *American Mineralogist* 84, 1741–1759.
- Ramsay, J., Huber, M., 1983. The techniques of modern structural geology. vol. 1. Strain Analysis. Academic Press, London.
- Ranalli, G., 1995. Rheology of the earth. Chapman & Hall.
- Reddy, S. M., Potts, G. J., Kelley, S. P., 2001.  $^{40}\text{Ar}/^{39}\text{Ar}$  ages in deformed potassium feldspar: Evidence of microstructural control on Ar isotope systematics. *Contributions to Mineralogy and Petrology* 141 (2), 186–200.
- Reddy, S. M., Timms, N. E., Trimby, P., Kinny, P. D., Buchan, C., Blake, K., 2006. Crystal-plastic deformation of zircon: A defect in the assumption of chemical robustness. *Geology* 34 (4), 257–260.
- Ruoff, A. L., Balluffi, R. W., 1963a. On strain-enhanced diffusion in metals II: Dislocation and grain boundary short-circuiting models. *Journal of Applied Physics* 34 (7), 1848–1853.
- Ruoff, A. L., Balluffi, R. W., 1963b. On strain-enhanced diffusion in metals II: Interpretation of recent experiments. *Journal of Applied Physics* 34 (9), 2862–2872.
- Rybacki, E., Dresen, G., 2004. Deformation mechanism maps for feldspar rocks. *Tectonophysics* 382 (3–4), 173–187.
- Sassier, C., Leloup, P. H., Rubatto, D., Galland, O., Yue, Y., Lin, D., 2009. Direct measurement of strain rates in ductile shear zones: A new method based on syntectonic dikes. *Journal of Geophysical Research: Solid Earth* 114, n/a–n/a.
- Schmidt, K., Paterson, S., Blythe, A., Kopf, C., 2009. Mountain building across a lithospheric boundary during arc construction: The Cretaceous Peninsular Ranges batholith in the Sierra San Pedro Martir of Baja California, Mexico. *Tectonophysics* 477 (3), 292–310.
- Simmons, J., Dorn, J. E., 1958. Analyses for Diffusion during Plastic Deformation. *Journal of Applied Physics* 29 (9), 1308–1313.
- Spear, F., 1993. Metamorphic phase equilibria and temperature–pressure–time paths. Mineralogical Society of America Monograph.
- Stipp, M., Stünitz, H., Heilbronner, R., Schmid, S. M., 2002. The eastern Tonale fault zone: A “natural laboratory” for crystal plastic deformation of quartz over a temperature range from 250 to 750°C. *Journal of Structural Geology* 24 (12), 1861–1884.
- Stipp, M., Tullis, J., 2003. The recrystallized grain size piezometer for quartz. *Geophysical Research Letters* 30 (21), 2088.
- Strandmann, P. A. E. P. v., Dohmen, R., Marschall, H. R., Schumacher, J. C., Elliott, T., 2015. Extreme magnesium isotope fractionation at outcrop scale records the mechanism and rate at which reaction fronts advance. *Journal of Petrology* 56 (1), 33–58.

- van Hinsberg, V. J., Henry, D. J., Dutrow, B. L., 2011. Tourmaline as a Petrologic Forensic Mineral: A Unique Recorder of Its Geologic Past. *Elements* 7 (5), 327–332.
- Van Orman, J. A., Grove, T. L., Shimizu, N., 2001. Rare earth element diffusion in diopside: influence of temperature, pressure, and ionic radius, and an elastic model for diffusion in silicates. *Contributions to Mineralogy and Petrology* 141 (6), 687–703.
- Vernon, R. H., 2000. Review of microstructural evidence of magmatic and solid-state flow. *Visual Geosciences* 5 (2), 1–23.
- Vernon, R. H., Johnson, S. E., Melis, E. A., 2004. Emplacement-related microstructures in the margin of a deformed pluton: the San José tonalite, Baja California, México. *Journal of Structural Geology* 26 (10), 1867–1884.
- Watanabe, T., Karashima, S., 1970. On the strain-enhanced diffusion of  $\alpha$ -iron. *Physica Status Solidi* 42 (2), 749–756.
- Wetmore, P. H., Schmidt, K. L., Paterson, S. R., Herzig, C., 2002. Tectonic implications for the along-strike variation of the Peninsular Ranges batholith, southern and Baja California. *Geology* 30 (3), 247–250.
- White, S. H., Burrows, S. E., Carreras, J., Shaw, N. D., Humphreys, F. J., 1980. On mylonites in ductile shear zones. *Journal of Structural Geology* 2 (1), 175–187.
- Yund, R. A., Smith, B. M., Tullis, J., 1981. Dislocation-assisted diffusion of oxygen in albite. *Physics and Chemistry of Minerals* 7 (4), 185–189.
- Zellmer, G., Sparks, R., Hawkesworth, C., Wiedenbeck, M., 2003. Magma emplacement and remobilization timescales beneath Montserrat: Insights from Sr and Ba zonation in plagioclase phenocrysts. *Journal of Petrology* 44 (8), 1413–1431.
- Zhang, Y., 2008. *Geochemical Kinetics*. Princeton University Press, Ch. Introduction and Overview, pp. 1–94.
- Zhang, Y., 2010. Diffusion in minerals and melts: Theoretical background. *Reviews in Mineralogy and Geochemistry* 72, 5–59.

# Appendices

---

## Calculation of strain energy contribution: MATLAB script

```
%  
% % Material Properties  
%  
mol = 6.022e23;  
  
A = 1.608; % Initial bond length in Å, here for Si-O in qtz at 200 MPa from  
% Levien et al. 1980, American Mineralogist  
  
% unit cell dimensions in Å (here for qtz, Levien et al., 1980)  
a = 4.8761;  
b = 4.8761;  
c = 5.37465;  
Z = 3; % atoms of Si per qtz formula unit  
  
Ym = 68; % Young's modulus (GPa) for qtz from Pabst and Gregorová (2013)  
  
% Activation energy in kJ/mol, here Si in qtz (Brady and Cherniak, 2010)  
E_a = 301;  
E_al = E_a - 14; % Uncertainty lower bound  
E_au = E_a + 14; % upper bound  
  
% How much strain?  
str = 0.01  
  
% Is this strain geologically reasonable at a large scale?  
Stress = Ym .* str % in GPa  
  
%  
% Calculate strain energy per volume from definition of elastic potential  
% energy  
%  
strbA = (str .* A); % bond length change in Å  
strbondlength = A + strbA; % strained bond length in Å  
strb = (str.*A) .* (10-10); % strained bond length in m  
Uem3 = (0.5) .* Ym .* ((str)2); % strain contribution in GPa/m3  
  
%  
% Convert to mol of diffusing species  
%  
V = a .* b .* c; % unit cell volume in Å3  
Vm = V .* (10-30); %unit cell vol in m3  
Conv = Vm .* mol ./Z; % conversion from m3 to mol of diffusant in lattice  
  
%  
% Convert strain contribution to kJ/mol to compare to D  
%
```

---

```

Ue = (Uem3.*10^6) .* Conv % total contribution in kJ/mol
PercentContribution = Ue/E_a .* 100;
Pl = 100 .* Ue ./ E_al; % bounds on this estimate
Pu = 100 .* Ue ./ E_au;

%
% Determine how much difference this makes on geologic scales
%

% specify conditions:
TC = 400; % desired T in °C
T = TC + 273; % T in K for calculation
R = 0.00831451; % Universal gas constant, (kJ) (K^-1) (mol^-1)
tyr = 10000; % time in years
t = tyr .* 31556900; % convert years to s

% set up parameters
E_reduc = E_a - Ue; % new activation energy in strained case
Do = 3.5941 .* (10^(-6)); % D_0 for Si diffusion in qtz (Brady and Chernaik, 2010)

% Diffusion rates:
D_undef = Do .* exp(-E_a ./ (R.*T)) % static diffusion coefficient
D_enh = Do .* exp(-E_reduc ./ (R.*T)) % enhanced diffusion coefficient
D_rel = 100.*(D_enh - D_undef)./D_undef % percent enhancement

% How much farther could an Si atom go?
% give some starting relative concentrations
C1 = 1;
C2 = 2;
% condition: C1 < C2 for erfinv to work

dist_undef = erfinv(C1./C2) .* sqrt(4.*D_undef .* t) .* 10^6 % distance in microns
dist_def = erfinv(C1./C2) .* sqrt(4.*D_enh .* t) .* 10^6 % distance in microns
dist_change = dist_def - dist_undef % in microns
Farther = 100.*((dist_def - dist_undef)./dist_undef) % percent farther

Results For Si in Qtz:

E_a = 301
str = 0.0100
Stress = 0.6800
Ue = 0.0872
D_undef = 1.5638e-29
D_enh = 1.5884e-29
D_rel = 1.5708
tyr = 10^6
dist_undef = 0.0212
dist_def = 0.0214

```

---

dist\_change = 1.6578e-04  
Farther = 0.7824

Results for Ar in Qtz, assuming same energy contribution:

E\_a = 47  
str = 0.0100  
Stress = 0.6800  
Ue = 0.0872  
D\_undef = 1.2567e-22  
D\_enh = 1.2764e-22  
D\_rel = 1.5708  
tyr = 10<sup>6</sup>  
dist\_undef = 60.0692  
dist\_def = 60.5391  
dist\_change = 0.4700  
Farther = 0.7824

Results for Li in Qtz

E\_a = 86  
str = 0.0100  
Stress = 0.6800  
Ue = 0.0872  
tyr = 10<sup>6</sup>  
Do = 6.9000e-07  
D\_undef = 1.4594e-13  
D\_enh = 1.4823e-13  
D\_rel = 1.5708  
dist\_undef = 2.0470e+06  
dist\_def = 2.0630e+06  
dist\_change = 1.6015e+04  
Farther = 0.7824